Liquid-induced topological transformations of cellular microstructures

https://doi.org/10.1038/s41586-021-03404-7

Received: 17 August 2020

Accepted: 1 March 2021

Shucong Li[1,3], Bolei Deng[2,3], Alison Grinthal[2], Alyssha Schneider-Yamamura[2], Jinliang Kang[2], Reese S. Martens[2], Cathy T. Zhang[2], Jian Li[2], Siqin Yu[2], Katia Bertoldi[2] & Joanna Aizenberg[1,2] ✉

The fundamental topology of cellular structures—the location, number and connectivity of nodes and compartments—can profoundly affect their acoustic[1–4], electrical[5], chemical[6,7], mechanical[8–10] and optical[11] properties, as well as heat[1,12], fluid[13,14] and particle transport[15]. Approaches that harness swelling[16–18], electromagnetic actuation[19,20] and mechanical instabilities[21–23] in cellular materials have enabled a variety of interesting wall deformations and compartment shape alterations, but the resulting structures generally preserve the defining connectivity features of the initial topology. Achieving topological transformation presents a distinct challenge for existing strategies: it requires complex reorganization, repacking, and coordinated bending, stretching and folding, particularly around each node, where elastic resistance is highest owing to connectivity. Here we introduce a two-tiered dynamic strategy that achieves systematic reversible transformations of the fundamental topology of cellular microstructures, which can be applied to a wide range of materials and geometries. Our approach requires only exposing the structure to a selected liquid that is able to first infiltrate and plasticize the material at the molecular scale, and then, upon evaporation, form a network of localized capillary forces at the architectural scale that 'zip' the edges of the softened lattice into a new topological structure, which subsequently restiffens and remains kinetically trapped. Reversibility is induced by applying a mixture of liquids that act separately at the molecular and architectural scales (thus offering modular temporal control over the softening–evaporation–stiffening sequence) to restore the original topology or provide access to intermediate modes. Guided by a generalized theoretical model that connects cellular geometries, material stiffness and capillary forces, we demonstrate programmed reversible topological transformations of various lattice geometries and responsive materials that undergo fast global or localized deformations. We then harness dynamic topologies to develop active surfaces with information encryption, selective particle trapping and bubble release, as well as tunable mechanical, chemical and acoustic properties.

Evaporating liquids have been shown to deform and assemble simple, isolated microscale structures, such as arrays of base-attached pillars and plates, via the capillary forces of the formed liquid–vapour menisci[24–27]. We anticipated that when a liquid is applied to a cellular structure, the formation of a complex network of menisci on the interconnected geometry generates an intricate localized force field centred at each node, providing a finer level of control than can be achieved with global force fields[19,20]. However, as a base-attached interconnected structure, a cellular lattice generally requires much higher energy to deform compared to that needed for simple bending in the isolated structures, usually making capillary forces too weak for such transitions. Although the capillarity-induced reconfiguration could potentially be enabled by using a floppy material with low elastic restoring energy[28] and high surface adhesion[26,29,30] to maintain the assembly, such systems are impractical for most applications. This apparent paradox can be resolved by introducing a transient softening of structures. It has been shown that certain liquids are able to infiltrate and soften polymeric materials at the molecular scale, thus altering their bulk mechanical properties[31–36].

On the basis of the latter considerations, we introduce a strategy to achieve fast, reversible and tunable topological transformation of cellular microstructures through capillary assembly that is broadly applicable to a wide range of geometries and materials. The key concept is that the applied liquid must not only form menisci at the architectural (micro)scale, as generally occurs in evaporation-induced assembly[24–27] (Fig. 1a), but must first transiently infiltrate, swell and plasticize the

---

[1] Department of Chemistry and Chemical Biology, Harvard University, Cambridge, MA, USA. [2] Harvard John A. Paulson School of Engineering and Applied Sciences, Harvard University, Cambridge, MA, USA. [3] These authors contributed equally: Shucong Li, Bolei Deng. ✉e-mail: jaiz@seas.harvard.edu

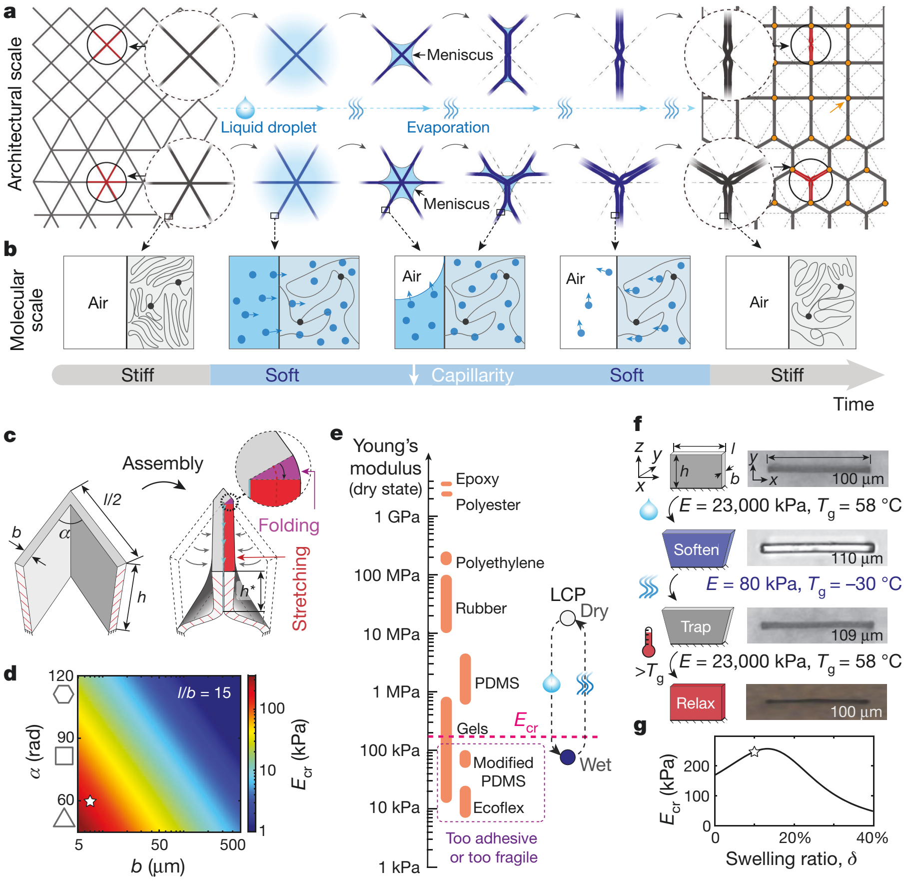

Fig. 1 | Strategy for topological transformation of cellular structures. a, **b**, Schematic illustration of topological transformation occurring at the architectural scale during liquid immersion and evaporation (**a**), and corresponding changes in the polymer network at the molecular scale (**b**). Because the liquid in the compartments evaporates before the liquid inside the polymer network, the capillary forces introduced at the air–liquid interface always act on the softened structure, enabling the structure to deform and the edges to be zipped together. This results in the formation of new nodes (shown in orange and indicated by the orange arrow on the right) and the disappearance or change in connectivity of the original nodes (shown in red). **c**, Schematics of the assembly of two adjacent walls from a cellular structure characterized by angle α, edge length l, thickness b and height h. The walls are stretched and folded by the capillary forces. **d**, Contour plot of critical Young's modulus E_{cr} with respect to structural parameters α and b, with the slenderness ratio fixed at $l/b = 15$. The star marker denotes the corresponding parameters of the considered structure. **e**, List of frequently used polymeric materials and their Young's moduli in a dry state. The Young's modulus of a dry LCP changes reversibly from 23,000 kPa to 80 kPa when plasticized. **f**, Micrographs of an LCP microplate with dimensions $l = 100$ μm, $b = 7$ μm and $h = 70$ μm after exposure to acetone. **g**, Critical modulus E_{cr} as a function of swelling ratio, δ. The star marker shows the swelling ratio of the selected material.

material (Fig. 1b). Critically, as the liquid begins to evaporate from inside the compartments, capillary forces are exerted on the softened structure, acting locally at each individual node and zipping the edges together in a coordinated manner. This leads to a change in the connectivity of the original nodes, or to their disappearance and the creation of new nodes, while also changing the number and coordination of compartments, resulting in transformation to a new lattice topology. Finally, as the liquid rapidly evaporates from inside the material at the molecular scale, the dried structure regains its stiffness and the new geometry remains trapped (Fig. 1b).

To quantitatively investigate such a topological transformation process and to determine the critical elasticity threshold required for full transformation to a new topology, a simplified mathematical model is developed. We focus on two adjacent walls forming an angle α as part of a general cellular structure with edge length l, thickness b and height h. After transformation by capillarity, only the upper portion with height h^* is assembled because the bottom of the structure is always attached to the base (Fig. 1c). This upper portion deformation results in stretching ($\propto b$) and folding ($\propto b^2$) of the walls, and dominates the total elastic energy relative to the bending deformation ($\propto b^3$) of the lower part; this assumption holds as long as the height of the structure h is not too small compared to the edge length l. On the other hand, the work done by capillarity is approximated by the capillary forces (γh^*) multiplied by the distance travelled by the menisci (($l/2$)sec($\alpha/2$)) (refs. [27,37,38]), where γ is the surface tension of the liquid. For the capillary assembly to happen, the capillary work must overcome the elastic energy; this simplified energy argument gives a critical Young's modulus for the underlying material (Supplementary Information section 2, Supplementary Fig. 1):

$$E_{cr} = \frac{6\gamma l \sec(\alpha/2)}{3lb[\sec(\alpha/2) - 1 - \delta]^2 + \alpha b^2(1+\delta)^2}, \qquad (1)$$

where δ is the swelling ratio of the material by the liquid. E_{cr} provides an upper limit for the material stiffness above which the transformation will not occur. In Fig. 1d, we present the evolution of E_{cr} as a function of angle α and wall thickness b (varying from 5 μm to 500 μm) for structures with a constant slenderness ratio of $l/b = 15$ and $\gamma = 25 \times 10^{-3}$ N m^{-1} (for typical volatile liquids, such as acetone). According to the contour plot, E_{cr} decreases drastically down to a few kilopascals with increasing b, indicating that the smallest dimensions (that is, the wall thickness b) of the considered structure must stay within the micrometre scale for reasonable material stiffness. Moreover, E_{cr} also decreases with increasing angle α, showing that structures with larger angles, such as square and hexagonal lattices, are much more difficult to transform than those with smaller angles.

Although our model can predict the assembly behaviour of a wide range of cellular architectures (Supplementary Fig. 2), we selected a triangular ($\alpha = 60°$) micro-cellular structure with dimensions $l = 100$ μm, $b = 7$ μm and $h = 70$ μm as an initial experimental test case. For such a structure, equation (1) provides a critical modulus of $E_{cr} \approx 175$ kPa, which is much lower than that of most commonly used polymers, such as polydimethylsiloxane (PDMS), rubber, polyethylene or epoxy (Fig. 1e). Although there exist soft materials with Young's modulus below E_{cr} (such as Ecoflex or PDMS with low crosslinking density[29], bottle-brush PDMS[28] and hydrogels[39]), they are too sticky or fragile to be compatible with the moulding fabrication procedure of high-aspect-ratio microstructures, and typically undergo permanent distortion after demoulding or irreversible collapse (Supplementary Fig. 3). By contrast, the transient solvent-induced softening allows topological transformation to be extended to polymers with high Young's modulus that can be easily moulded, temporarily plasticized during assembly and restiffened after evaporation. Key features in selecting a polymer–solvent pair suitable for topological transformation are the solubility, volatility and Flory–Huggins parameters[31–33,35], which describe the ability of the

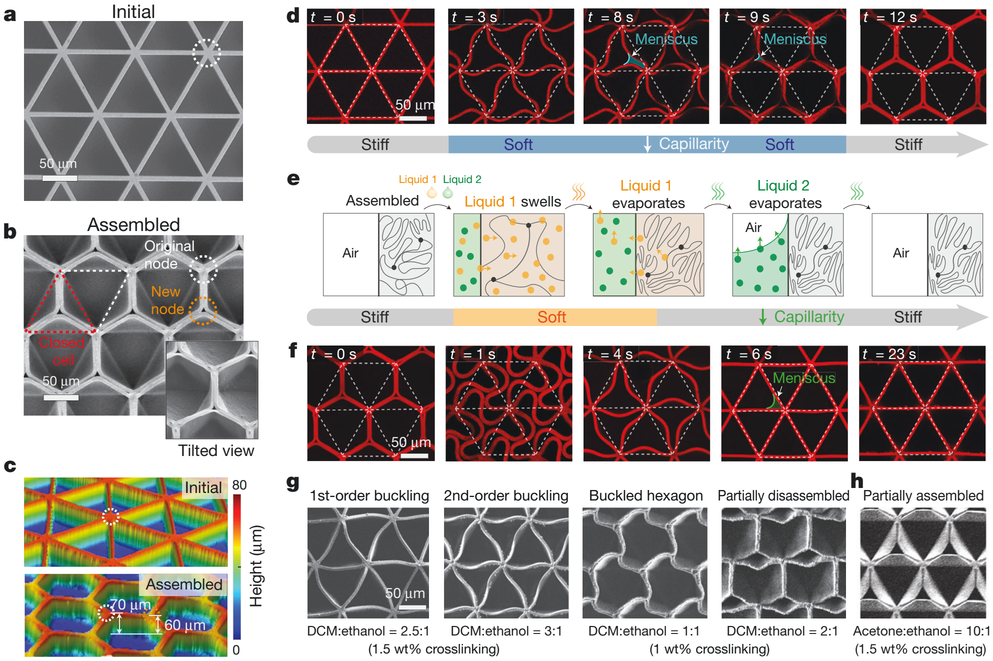

Fig. 2 | Experimental characterization of the assembly and disassembly of a triangular lattice. a, Top view of the initial triangular micro-cellular structure, imaged by a scanning electron microscope. **b**, Top and tilted views of the assembled micro-cellular structure. The initial triangular lattice is transformed to a hexagonal lattice upon application of an acetone droplet (~50 µl for a ~1 cm^2 sample). One of the new nodes is marked with an orange circle and an original node with a white circle. **c**, Profilometer 3D surface topography of the initial (top) and assembled (bottom) microstructure. Whereas the top surface of the original structure is planar, the assembled structure contains nodes of two different heights owing to the wall deformation. **d**, Fluorescence confocal images of the microstructures at different stages of the assembly. Rhodamine B was co-polymerized into the polymer for characterization by fluorescence confocal microscopy (Supplementary Information section 1.2). **e**, Schematic representation of the generalized mechanism of the disassembly process, showing how the mixture of two liquids decouples the two scales, with one—highly volatile—liquid acting at the molecular scale and another—chemically inert, less volatile—liquid returning the structure to its original state at the micrometre scale. **f**, Fluorescence confocal images of the LCP microstructures at different stages during the disassembly induced by the DCM:ethanol mixture at 2:1 ratio, with DCM swelling the assembled structure considerably to disassociate the assembled walls, and ethanol exerting capillary forces on a stiffened structure after evaporation of DCM. **g**, Selective trapping of intermediate stages (imaged by a scanning electron microscope) by tuning the evaporation kinetics using different solvent concentrations and polymer compositions. All the presented structures are transformed from the assembled hexagonal lattice (as shown in Fig. 2b). **h**, Partial topological transformation of the initial triangular lattice into a hierarchical triangular lattice with two compartment sizes using a mixture of acetone and ethanol.

solvent to swell and soften the elastic network below E_{cr}, whereas high volatility allows fast transformation. In addition, the properties of the polymer matrix, including the chemical nature, crosslinking density, crystallization (molecular packing/physical crosslinking), porosity, and chain topology[34,36], can be leveraged to modify the solvent–polymer interaction.

As a representative material, a polydomain liquid-crystalline polymer (LCP) with an initial modulus of about 23,000 kPa in the dry state (far above E_{cr}) was selected as a model system (Fig. 1e, Supplementary Fig. 4a). To focus on the material properties of the LCP during the liquid treatment while eliminating complex assembly behaviour, an isolated base-attached LCP microplate was fabricated with the same dimensions as an edge of the considered lattice structure to ensure comparable dynamics and kinetics of evaporation (Fig. 1f). When the plate is swelled by the wetting liquid acetone—a good solvent of the LCP, with a vapour pressure of 30.7 kPa at 25 °C—the solvent molecules penetrate into the polymer matrix, break the packing of the polymer chains and plasticize the material[35,40], reducing the glass transition temperature (T_g) from 58 °C to −30 °C and softening the material drastically down to about 80 kPa (Supplementary Fig. 5), while also swelling the plate to a 10% strain along the top edge. Upon evaporation, T_g returns to 58 °C as the material returns to its original stiffness of about 23,000 kPa, and the dried plate is kinetically trapped with a 9% strain in the glassy state at room temperature; the extended conformation of polymer chains in the swollen state is locked owing to the fast evaporation of liquid in the microscopic system[41,42]. The plate can relax back to its initial length when heated above T_g as the polymer chains return to the original conformation (Fig. 1f, Supplementary Video 1). According to our theoretical model, such swelling of the material facilitates assembly because it compensates for the required stretching of the walls, and trapping plays a critical role in maintaining the assembly after the capillary force ceases (Fig. 1g). Trapping is expected to occur for materials that have a dry-state T_g that is higher than the ambient temperature. Without this effect, an approximate adhesion energy of 3.3 J m^{-2} would be required to hold the restiffened structure together (Supplementary Information section 2.3), which is much higher than the adhesion energy of typically used materials[43,44].

To test our strategy, the triangular cellular microstructure was moulded from LCP by soft lithography (Fig. 2a). Droplets of acetone were placed on horizontal substrates to immerse the cellular structure and allowed to evaporate under ambient conditions (for a systematic study of other liquids, see Supplementary Fig. 6). After evaporation, the upper portion of the triangular lattice was transformed to hexagonal, with triangular geometry retained at the base (Fig. 2b). The transformation results in the change of the fundamental topology of the microstructure: the node connectivity changes from six to three, the number of compartments is halved, and the number of nodes and size of compartments are doubled. Additionally, according to optical three-dimensional (3D) surface profilometry (Fig. 2c, Supplementary Fig. 7), the initial two-dimensional (2D) lattice becomes a true 3D structure with a non-planar top surface after the assembly, owing to the formation of enclosures and a more complex height profile, given

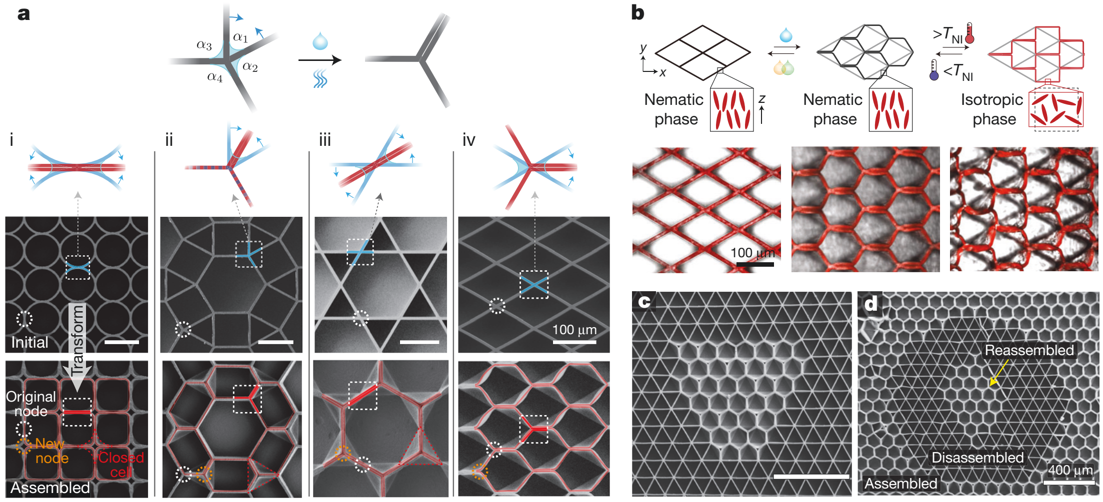

Fig. 3 | Generalization of topological transformation principle. a, The generalized lattice consists of nodes with different angles. The edges forming the smallest angle will undergo zipping for angle-guided capillary-driven transformations from: circular to square (i), rhombitrihexagonal to hybrid hexagonal (ii), kagome to hexagonal (iii) and rhombic to hexagonal (iv). We note that, compared to the triangular-transformed and kagome-transformed hexagonal lattices, which are comprised of nodes connecting three equal double walls, nodes in the hexagonal lattice assembled from the diamond structure comprise two single walls and one double wall, resulting in additional anisotropy along the horizontal direction. **b**, Multi-stimuli deformation of molecularly aligned LCP diamond-shaped cellular structures with the director oriented along the *z* axis. **c**, **d**, Regional triangular–hexagonal transformations through localized multi-step assembly/disassembly.

that the new nodes formed by the inward-bending plates are 10 µm shorter than the original nodes.

The dynamics of the assembly process was monitored by fluorescent confocal microscopy (Fig. 2d, Supplementary Video 2). Acetone first swells the material, leading to a buckled configuration (at time $t = 3$ s), and upon evaporation forms menisci, where the localized capillary forces break the symmetry of each node ($t = 8$ s). The menisci further zip up the buckled walls and ultimately transform the node connectivity from six to three ($t = 9$ s) with neighbouring nodes transforming coordinately, forming ordered domains (Supplementary Fig. 8). Finally, as the material de-swells, the structure is locked in the hexagonal topology with straightened double walls ($t = 12$ s). Both trapping of the material and adhesion between the assembled walls contribute to retaining the new topology, which remains robust under harsh conditions, including heating above T_g or immersing in various non-swelling liquids for several days (Supplementary Fig. 9, Supplementary Video 3).

Disassembling the structure and restoring the original topology requires overcoming both the kinetic trapping of the polymer conformation and the interfacial adhesion between the walls. Although heat or plasticizers can untrap the material, they also tend to decrease the elastic restoring force. Both requirements can be fulfilled simultaneously by applying a liquid that swells the underlying material with a much greater swelling ratio than that of the liquid used for the assembly, to trigger drastic bending of the assembled walls that overcomes the adhesion and leads to the dissociation of the walls, initiating disassembly. However, as the liquid evaporates, the formed menisci would tend to reassemble the structure. To reduce the capillary forces, a second liquid—less volatile, but non-swelling—is mixed with the first one to delay any capillary forces until after the material has finished disassembling and has become stiff again (Fig. 2e). To demonstrate this unique disassembly mechanism experimentally, we used a mixture of dichloromethane (DCM)—a good solvent of LCP, that swells the LCP substantially (with >30% strain)—as the first volatile liquid (vapour pressure of 57.3 kPa at 25 °C) and ethanol—a poor solvent of the LCP—as the second, less volatile liquid (vapour pressure of 5.95 kPa at 25 °C) (Fig. 2f, Supplementary Video 4). Compared to the assembly process in which a single liquid both softens the material at the molecular scale and generates capillary forces at the architectural scale, the mixture enables modular control over the timescales of the two actions, with DCM controlling the molecular scale and ethanol governing the architectural scale separately and consecutively to yield desired outcomes.

In addition to restoring the original triangular structure, such modular control enables trapping of a series of intermediate states during disassembly by varying the DCM–ethanol ratio, which affects both the swelling extent of the LCP and the volatility of DCM when dispersed in ethanol, and thus the trapping strain and modes of disassembly (Fig. 2g). Similar concepts can also be used to tailor the original assembly process. For example, Fig. 2h shows that partial assembly of the triangular lattice can be achieved by adding to acetone a trace amount of ethanol, which diminishes the softening effect and increases the elastic restoring energy during assembly. Notably, the assembly and disassembly processes take only seconds and are highly reversible and fatigue-free (Supplementary Fig. 10), enabling a durable and fast switching between different topologies of microstructures.

The methodology can be generalized to different geometries with more complex symmetries, anisotropies, and combinations of compartment shapes and sizes. An arbitrary lattice can be considered as a combination of nodes connected to edges that form different angles, with the capillary forces preferentially assembling edge pairs with smaller angles (Fig. 3a). On the basis of this principle, we designed and experimentally tested a variety of cellular architectures undergoing programmed, robust topological transitions (Fig. 3a, Supplementary Fig. 11). The approach is also readily applicable to structures with different dimensions and to other polymeric materials (Supplementary Figs. 12, 13). It can also be integrated with orthogonal response mechanisms to enable multimodal transformations of a given lattice upon application of different triggers. For example, LCPs can be imprinted with anisotropic thermal responses by aligning the liquid-crystal molecules inside the cellular structures into a nematic liquid-crystalline phase (Supplementary Fig. 13b)[45,46]. Figure 3b presents an exemplary diamond lattice with the liquid-crystal director aligned perpendicular to the base[47] that is transformed to a hexagonal lattice via capillary assembly, and then to a brick pattern by heating to above its thermal nematic-to-isotropic phase-transition temperature ($>T_{NI}$) (Supplementary Video 5). We further note that the presented strategy is applicable to any 2D or 3D

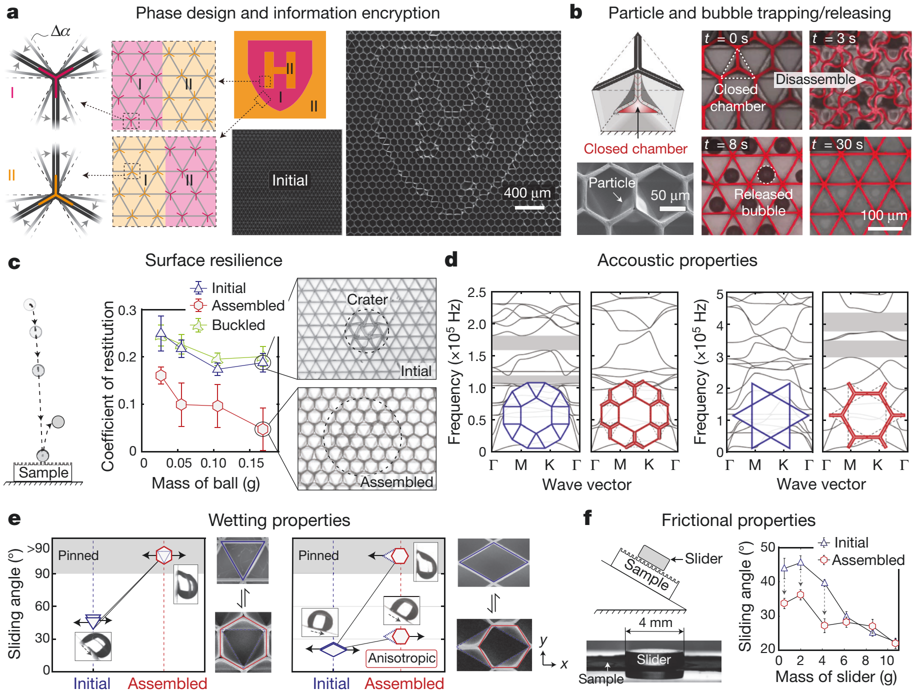

Fig. 4 | Exemplary applications of lattice structures undergoing topological transformations. a, Information encryption. Harvard shield outlined by the engineered phase boundaries appears upon topological transformation of the triangular lattice. **b**, Particle and bubble trapping/releasing through the closed chambers formed by topological transformation. **c**, Ball bouncing test carried out to measure the resilience of the surface before and after transformation. Error bars represent the standard deviation of eight measurements. We note that the topological transformation is necessary to change the coefficient of restitution, as simply buckled (presented in Fig. 2g) and undeformed structures show the same resilience. **d**, Bandgaps can be tuned by capillarity-driven assembly for some lattices. Examples for bandgaps in rhombitrihexagonal and kagome lattices are shown. **e**, **f**, Controlling surface properties upon topological transformations: wetting (**e**); friction (**f**). Error bars represent the standard deviation of three measurements.

geometries, including base-attached or free-standing ones (see Supplementary Fig. 14). Here we intentionally choose a rigid-base-attached configuration for its better structural stability, applicability to any lattice geometry, and the ability to form closed cavities upon topological transformation—a unique compartmentalization feature explored in applications described below. Moreover, we demonstrate interesting region-specific assembly–disassembly transformations through the application of small droplets locally—another property unachievable with global fields (Fig. 3c, d, Supplementary Fig. 15).

By carefully programming the spatial distribution of angular perturbations at each node, we can eliminate or engineer the location of domain boundaries in assembled structures (Supplementary Information section 3.8, Supplementary Figs. 16, 17, Supplementary Video 6). Considering the large triangular lattice shown in Fig. 4a, the nodes inside the magenta region are designed to transition to Y-shaped (phase I), and the nodes inside the orange region are programmed to transition to inverted Y-shaped (phase II). The written-in phase information is not optically visible before assembly, and becomes evident only after solvent treatment (Fig. 4a, Supplementary Fig. 17). The information encryption and read-out can be reversed by treating the LCP microstructure with different solvent systems as discussed previously. We note that the location information of the designed phase boundaries is not merely stored on the phase boundaries, but encoded in every node of the structure via their preferred phase, which makes such information encryption extremely robust.

Topological changes of the cellular surfaces—such as the closure of subsets of compartments and the ability to induce global or localized transformations—provide opportunities for a number of applications. As shown in Fig. 4b, the cellular surface can selectively trap and sort microparticles with diameters <50 µm that are able to enter the initially triangular compartment. Furthermore, the closed chambers also create ordered cavities that each capture and release uniform microscale bubbles upon assembly–disassembly (Fig. 4c, Supplementary Video 7) that can be used as miniaturized chemical reaction chambers. The resilience of the cellular surface also changes considerably after the topological transformation, as demonstrated by the ball-bouncing test results (Fig. 4d, Supplementary Video 7). Compared to the uniform or buckled triangular structure that displays broken walls upon impact, the transformed hexagonal surface exhibits larger craters with no detectable structural damage. We believe that the formed closed chambers constitute a cushion layer and offer extra structural flexibility, which increases the efficiency in absorbing the impact energy.

The change of geometry, combined with the formation of double walls, also serves as a platform for tunable phononic crystals, in which the bandgaps and propagation velocity of elastic waves can be altered reversibly (Fig. 4e). As noted above, the 3D height profile of the structure is also changed through edge assembly and node formation (Fig. 2c), giving rise to modified surface planarity and anisotropy that affect surface properties such as wetting and friction (Fig. 4f), and both surface properties can be further changed by localized, areal topological transformations. For example, the surface becomes much more adhesive to water droplets when transformed from a triangular to a non-planar hexagonal lattice (Supplementary Video 7), which can most probably be attributed to the pinning points that are created when new nodes form and to the overall elongation of walls that causes the water–polymer contact area to increase slightly. Moreover, anisotropic, directional wetting properties can be achieved through a diamond-to-hexagon transformation in which the initial diamond lattice shows an isotropic wetting along the *x* axis, but after assembly the sliding angle towards the left is much higher (>90°, pinned) than towards the right (~34°). This can be explained by the asymmetric tetrahedral containers formed by the slanted walls that pin the left-travelling droplet to the surface. Similarly, the friction coefficient of the cellular surface is also tunable via topological transformations (Fig. 4g).

In conclusion, we have presented a simple, widely applicable strategy that gives rise to complex topological transformations of cellular microstructures. The defining feature of our approach is that the applied liquid has a dual role by acting at two scales: it transiently softens and swells the material at the molecular level and creates an intricate network of localized capillary forces at the architectural scale, and these actions at two scales take place in a sequentially controlled manner. Modular control over the timing and extent of the softening/restiffening/evaporation events through customized polymer–liquid pairs enables reversibility and switching between various intermediate topologies. Our theoretical model provides a quantitative foundation for rationally guiding the materials selection and structural design. Compared to existing reconfiguration methods—which produce buckling or shearing deformations without controllable topological changes[16–23]; are often either irreversible or unable to hold the reconfigured shape without external stimuli[16,18,19]; or require complex material compositions, sophisticated and costly fabrication procedures that are not applicable at the microscale[17,19,20], and/or long response times[18,20]—our strategy enables extremely fast, robust and reversible topological transformations and is compatible with a simple moulding fabrication procedure. The demonstrated applications can be integrated with global or localized transformations, phase boundary design and active materials responding to orthogonal stimuli, to control functional properties across different scales and application fields. In principle, our strategy can be applied to nanoscale structures and will open avenues for designing tunable photonic meta-surfaces in which the topology has a key role. The opportunities offered by this strategy to systematically manipulate the topological transformation provide a platform for the fundamental study of the topology–dimension–material relation and the underlying multiscale physicochemical mechanisms.

Online content

Any methods, additional references, Nature Research reporting summaries, source data, extended data, supplementary information, acknowledgements, peer review information; details of author contributions and competing interests; and statements of data and code availability are available at https://doi.org/10.1038/s41586-021-03404-7.

1. Gibson, L., Ashby, M. & Harley, B. *Cellular Materials in Nature and Medicine* (Cambridge Univ. Press, 2010).
2. Gibson, L. J. & Ashby, M. F. *Cellular Solids: Structure, Properties and Applications* (Cambridge Univ. Press, 1999).
3. Ruzzene, M., Scarpa, F. & Soranna, F. Wave beaming effects in two-dimensional cellular structures. *Smart Mater. Struct*. **12**, 363–372 (2003).
4. He, H. et al. Topological negative refraction of surface acoustic waves in a Weyl phononic crystal. *Nature* **560**, 61–64 (2018).
5. Kang, S. et al. Stretchable lithium-ion battery based on re-entrant micro-honeycomb electrodes and cross-linked gel electrolyte. *ACS Nano* **14**, 3660–3668 (2020).
6. Shirman, E. et al. Modular design of advanced catalytic materials using hybrid organic–inorganic raspberry particles. *Adv. Funct. Mater*. **28**, 1704559 (2018).
7. Kim, O. H. et al. Ordered macroporous platinum electrode and enhanced mass transfer in fuel cells using inverse opal structure. *Nat. Commun*. **4**, 2473 (2013).
8. Muth, J. T., Dixon, P. G., Woish, L., Gibson, L. J. & Lewis, J. A. Architected cellular ceramics with tailored stiffness via direct foam writing. *Proc. Natl Acad. Sci. USA* **114**, 1832–1837 (2017).
9. Christensen, R. M. Mechanics of low density materials. *J. Mech. Phys. Solids* **34**, 563–578 (1986).
10. Coulais, C., Sabbadini, A., Vink, F. & van Hecke, M. Multi-step self-guided pathways for shape-changing metamaterials. *Nature* **561**, 512–515 (2018).
11. Gan, Z., Turner, M. D. & Gu, M. Biomimetic gyroid nanostructures exceeding their natural origins. *Sci. Adv*. **2**, e1600084 (2016).
12. Maloney, K. J. et al. Multifunctional heat exchangers derived from three-dimensional micro-lattice structures. *Int. J. Heat Mass Transf*. **55**, 2486–2493 (2012).
13. Khan, M. I. H., Farrell, T., Nagy, S. A. & Karim, M. A. Fundamental understanding of cellular water transport process in bio-food material during drying. *Sci. Rep*. **8**, 15191 (2018).
14. Zhang, R., Hao, P., Zhang, X. & He, F. Dynamics of high Weber number drops impacting on hydrophobic surfaces with closed micro-cells. *Soft Matter* **12**, 5808–5817 (2016).
15. Kim, J. J., Bong, K. W., Reátegui, E., Irimia, D. & Doyle, P. S. Porous microwells for geometry-selective, large-scale microparticle arrays. *Nat. Mater*. **16**, 139–146 (2017).
16. Kang, S. H., Shan, S., Noorduin, W. L., Khan, M., Aizenberg, J. & Bertoldi, K. Buckling-induced reversible symmetry breaking and amplification of chirality using supported cellular structures. *Adv. Mater*. **25**, 3380–3385 (2013).
17. Boley, J. W. et al. Shape-shifting structured lattices via multimaterial 4D printing. *Proc. Natl Acad. Sci. USA* **116**, 20856–20862 (2019).
18. Zhang, H., Guo, X., Wu, J., Fang, D. & Zhang, Y. Soft mechanical metamaterials with unusual swelling behavior and tunable stress-strain curves. *Sci. Adv*. **4**, eaar8535 (2018).
19. Kim, Y., Yuk, H., Zhao, R., Chester, S. A. & Zhao, X. Printing ferromagnetic domains for untethered fast-transforming soft materials. *Nature* **558**, 274–279 (2018).
20. Xia, X. et al. Electrochemically reconfigurable architected materials. *Nature* **573**, 205–213 (2019).
21. Coulais, C., Teomy, E., De Reus, K., Shokef, Y. & van Hecke, M. Combinatorial design of textured mechanical metamaterials. *Nature* **535**, 529–532 (2016).
22. Haghpanah, B., Salari-Sharif, L., Pourrajab, P., Hopkins, J. & Valdevit, L. Multistable shape-reconfigurable architected materials. *Adv. Mater*. **28**, 7915–7920 (2016).
23. Fu, H. et al. Morphable 3D mesostructures and microelectronic devices by multistable buckling mechanics. *Nat. Mater*. **17**, 268–276 (2018).
24. Bico, J., Roman, B., Moulin, L. & Boudaoud, A. Elastocapillary coalescence in wet hair. *Nature* **432**, 690 (2004).
25. Pokroy, B., Kang, S. H., Mahadevan, L. & Aizenberg, J. Self-organization of a mesoscale bristle into ordered, hierarchical helical assemblies. *Science* **323**, 237–240 (2009).
26. Kang, S. H., Pokroy, B., Mahadevan, L. & Aizenberg, J. Control of shape and size of nanopillar assembly by adhesion-mediated elastocapillary interaction. *ACS Nano* **4**, 6323–6331 (2010).
27. Roman, B. & Bico, J. Elasto-capillarity: deforming an elastic structure with a liquid droplet. *J. Phys. Condens. Matter* **22**, 493101 (2010).
28. Cai, L. H. et al. Soft poly(dimethylsiloxane) elastomers from architecture-driven entanglement free design. *Adv. Mater*. **27**, 5132–5140 (2015).
29. Jeong, S. H., Zhang, S., Hjort, K., Hilborn, J. & Wu, Z. PDMS-based elastomer tuned soft, stretchable, and sticky for epidermal electronics. *Adv. Mater*. **28**, 5830–5836 (2016).
30. Matsunaga, M., Aizenberg, M. & Aizenberg, J. Controlling the stability and reversibility of micropillar assembly by surface chemistry. *J. Am. Chem. Soc*. **133**, 5545–5553 (2011).
31. Flory, P. J. *Principles of Polymer Chemistry* (Cornell Univ. Press, 1953).
32. Rubinstein, M. & Colby, R. H. *Polymer Physics* (Oxford Univ. Press, 2003).
33. Dimarzio, E. A. & Gibbs, J. H. Molecular interpretation of glass temperature depression by plasticizers. *J. Polym. Sci. A* **1**, 1417–1428 (1963).
34. Lin, H. et al. Organic molecule-driven polymeric actuators. *Macromol. Rapid Commun*. **40**, 1800896 (2019).
35. Du, H. & Zhang, J. Solvent induced shape recovery of shape memory polymer based on chemically cross-linked poly(vinyl alcohol). *Soft Matter* **6**, 3370–3376 (2010).
36. Gu, Y., Zhao, J. & Johnson, J. A. Polymer networks: from plastics and gels to porous frameworks. *Angew. Chem. Int. Ed*. **59**, 5022–5049 (2020).
37. Holmes, D. P., Brun, P. T., Pandey, A. & Protière, S. Rising beyond elastocapillarity. *Soft Matter* **12**, 4886–4890 (2016).
38. Wei, Z. et al. Elastocapillary coalescence of plates and pillars. *Proc. R. Soc. A Math. Phys. Eng. Sci*. **471**, 20140593 (2015).
39. Calvert, P. Hydrogels for soft machines. *Adv. Mater*. **21**, 743–756 (2009).
40. Chow, T. S. Molecular interpretation of the glass transition temperature of polymer-diluent systems. *Macromolecules* **13**, 362–364 (1980).
41. Rath, A., Geethu, P. M., Mathesan, S., Satapathy, D. K. & Ghosh, P. Solvent triggered irreversible shape morphism of biopolymer films. *Soft Matter* **14**, 1672–1680 (2018).
42. Zhu, X., Wu, G., Dong, R., Chen, C. M. & Yang, S. Capillarity induced instability in responsive hydrogel membranes with periodic hole array. *Soft Matter* **8**, 8088–8093 (2012).
43. Myshkin, N. & Kovalev, A. Adhesion and surface forces in polymer tribology—a review. *Friction* **6**, 143–155 (2018).
44. Israelachvili, J. N. *Intermolecular and Surface Forces* (Academic Press, 2011).
45. White, T. J. & Broer, D. J. Programmable and adaptive mechanics with liquid crystal polymer networks and elastomers. *Nat. Mater*. **14**, 1087–1098 (2015).
46. Ohm, C., Brehmer, M. & Zentel, R. Liquid crystalline elastomers as actuators and sensors. *Adv. Mater*. **22**, 3366–3387 (2010).
47. Yao, Y. et al. Multiresponsive polymeric microstructures with encoded predetermined and self-regulated deformability. *Proc. Natl Acad. Sci. USA* **115**, 12950–12955 (2018).

Data availability

The data supporting the findings of this study are included within the paper and its Supplementary Information files and are available from the corresponding author upon reasonable request.

Acknowledgements This work was supported by the National Science Foundation (NSF) through the Designing Materials to Revolutionize and Engineer our Future (DMREF) programme under award number DMR-1922321 and the Harvard University Materials Research Science and Engineering Center (MRSEC) under award number DMR-2011754 (theory and computational studies), and by the US Department of Energy (DOE), Office of Science, Basic Energy Sciences (BES) under award number DE-SC0005247 (experiment and characterization). Microfabrication and scanning electron microscopy were performed at the Center for Nanoscale Systems (CNS) at Harvard, a member of the National Nanotechnology Coordinated Infrastructure Network (NNCI), which is supported by the NSF under NSF ECCS award number 1541959. We thank D. Y. Kim for fruitful discussions.

Author contributions S.L., B.D., K.B. and J.A. conceived and initiated the project. S.L., A.S.-Y., J.K., R.S.M. and C.T.Z. performed the experiments. B.D. performed the theoretical modelling and image analysis. J.L. and S.Y. performed the finite-element modelling and pattern designs. S.L., B.D. and A.G. analysed the experimental data. K.B. and J.A. supervised the project. All co-authors provided useful feedback and contributed to the manuscript.

Competing interests The authors declare no competing interests.

Additional information

Supplementary information The online version contains supplementary material available at https://doi.org/10.1038/s41586-021-03404-7.

Correspondence and requests for materials should be addressed to J.A.

Peer review information *Nature* thanks Robin Ras, Arnaud Saint-Jalmes, Scott Waitukaitis and the other, anonymous, reviewer(s) for their contribution to the peer review of this work. Peer reviewer reports are available.

nature portfolio

https://doi.org/10.1038/s41586-021-03404-7

Supplementary information

Liquid-induced topological transformations of cellular microstructures

Supplementary Materials for

Liquid-induced topological transformations of cellular microstructures

Shucong Li[1,†], Bolei Deng[2,†], Alison Grinthal[2], Alyssha Schneider-Yamamura[2], Jinliang Kang[2], Reese S. Martens[2], Cathy T. Zhang[2], Jian Li[2], Siqin Yu[2],

Katia Bertoldi[2], Joanna Aizenberg[1,2]

[1]Department of Chemistry and Chemical Biology,

Harvard University, Cambridge, Massachusetts 02138, USA

[2]Harvard John A. Paulson School of Engineering and Applied Sciences, Harvard University, Cambridge, Massachusetts 02138, USA

[†]These two authors contributed equally

[*]To whom correspondence should be addressed;

E-mail: jaiz@seas.harvard.edu

This Supplementary Information document includes:

Materials and Methods

Theoretical Model

Supplemental Results & Figures

Figs. S1 to S17

Captions for Supplementary Videos S1 to S7

Other Supplementary Material for this manuscript includes the following:

Videos S1 to S7 (.mp4)

Table of Contents

5 **References**

1 Materials and methods

1.1 Materials

The monomer **1** 4-(6-Acryloxy-hex-1-yl-oxy)phenyl 4-(hexyloxy)benzoate was purchased from Synthon Chemicals (ST03457). Photoinitiator Darocur®1173 (bis(2,4,6-trimethylbenzoyl) phenyl-phosphineoxide) was purchased from Sigma-Aldrich. 1,6-Hexanediol diacrylate (HDDA, crosslinker **2**) was purchased from Sigma-Aldrich, and the inhibitor was removed prior to use. Fluorescence label for confocal microscopy Methacryloxyethyl thiocarbamoyl rhodamine B dye was purchased from Polysciences, Inc.

The monomer (4″-acryloyloxybutyl 2,5-di(4′-butyloxybenzoyloxy) benzoate) used for the aligned LCP cellular structure was synthesized following a previously published procedure[1]. For magnetic alignment of the liquid crystal molecules, the high-temperature neodymium magnets (NdFeB, Grade N42SH; 1¨×1/2¨×1/2¨ thick; BX088SH) were purchased from K&J Magnetics, Inc.

For the control experiment with very soft materials, Ecoflex™ 00-10, and Ecoflex™ 00-50 were purchased from Smooth-on, Inc.

The monomer 2-Hydroxyethyl methacrylate and ethylene glycol dimethacrylate (EDGMA) for synthesizing poly(2-hydroxyethyl methacrylate) (PHEMA) were purchased from Sigma-Aldrich.

2,5-dihydroxybenzoic acid, benzyl bromide, 4-butyloxybenzoic acid, 4-hydroxybutyl acrylate, *N,N'*-dicyclohexylcarbodiimide (DCC), sodium bicarbonate ($NaHCO_3$), palladium on carbon (10 wt%, matrix activated), 4-pyrrolidinopyridine, Silica gel (Davisil Grade 633, high-purity grade, pore size 60 Å, 200-425 mesh particle size), and glacial acetic acid were purchased from Sigma-Aldrich.

Organic liquids including acetone, ethanol, isopropanol, used for testing assembly behavior were purchased from Macron. Organic liquids, including dichloromethane, toluene, dichloromethane, hexane, and toluene, were purchased from Sigma-Aldrich. Deionized water was used for aqueous systems.

4-inch Silicon wafers and 6-inch silicon-dioxide carriers were purchased from Nova Electronic Materials. Photoresist SPR220-7.0 was purchased from Microchem. Sylgard® 184 silicone kit was purchased from Ellsworth Adhesive Systems and used as 10:1 (Sylgard® base to curing agent). Microscopy glass slides (25×75 mm, 1 mm in thickness) were obtained from VWR.

1.2 Methods

UV-polymerization was conducted with a Dymax Model 2000 Flood UV Curing System chamber (light intensity of ~18 mW/cm^2) with a custom-made steel-mesh (as neutral density filter).

Differential scanning calorimetry (DSC) was performed on a Thermal Analysis (TA) DSC Q200 instrument to analyze the phase behaviors of the LC mixture and LCP in the dry and wet states under a nitrogen atmosphere. The program consisted of three cycles from –5 °C to 130 °C with a 10 °C/min rate for the LC mixtures, three cycles from –5 °C to 200 °C with a 10 °C/min rate for the LCP in the dry state, and three cycles from –80 °C to 50 °C with a 10 °C/min rate for the LCP in the wet state.

Scanning electron microscopy (SEM) of the Si master and LCP cellular microstructures was performed on a Zeiss Supra55VP Field Emission Scanning Electron Microscope (FESEM). The tilted view was taken with the SEM holder tilted 30° on a Zeiss Supra55VP FESEM. LCP cellular microstructures were coated with 10 nm Pt/Pd prior to imaging for increasing the conductivity of the polymeric surface.

Atomic force microscopy (AFM) was used to measure the Young's moduli of the LCP materials on a JPK Instruments NanoWizard®AFM with 240AC-NA tips (NANOANDMORE, USA, OP240AC-NA-10, force constant 2 N/m). In this technique, the deflection of the cantilever tip is measured as it approaches and indents the surface. The Young's moduli of the LCP material were determined through analyzing the slope of the force-displacement curves that result from these measurements while LCP is in the dry state and in the saturated swollen state.

Profilometer 3D profile was measured on a Veeco Dektak 6M profilometer. LCP cellular microstructures were coated with 10 nm Au prior to imaging for increased contrast.

Confocal laser scanning microscopy measurements were performed on a Zeiss LSM 700 instrument with 5× and 10× objectives under bright light channel and 532 nm fluorescence channel. LCP was copolymerized with the dye methacryloxyethyl thiocarbamoyl rhodamine B for fluorescence signal. Time-series was analyzed with the Zeiss ZEN black software.

Fabrication of microstructured silicon masters. The microstructured silicon master was produced by photolithography followed by reactive ion etching (RIE). Photoresist (SPR220-7.0) patterning was performed by UV exposure at 375 nm, 470 mJ/cm^2, under a Heidelberg MLA150 Maskless Aligner, which later served as the mask for the anisotropic etching of a Si wafer using an STS ICP RIE System, to obtain the Si microstructures. After removal of the photoresist with oxygen plasma, the Si master was treated with trichloro(*1H,1H,2H,2H*-perfluorooctyl) silane to render the structure hydrophobic for molding. Silicon master with positive cellular structure was designed for fabricating LCP microstructure and with negative cellular structure (micropost with gaps) was designed for fabricating silicone-based (i.e., Ecoflex™ 00-10, Ecoflex™ 00-50) microstructure.

Fabrication of PDMS negative molds. The polydimethylsiloxane (PDMS) precursor (mixture of Sylgard® 184 base and the crosslinker with the ratio of 10:1 (wt:wt)) was applied on top of the Si wafer, degassed under vacuum and cured at 70 °C for 2 h. Finally, the PDMS was cooled down to room temperature and carefully peeled off from the Si wafer and used as a mold for the synthesis of LCP microstructures.

Fabrication of Ecoflex™ 00-10 and Ecoflex™ 00-50 microstructures. The Ecoflex™ 00-10 or Ecoflex™ 00-50 precursor (part A and part B 1:1 by volume) were mixed thoroughly and applied on top of the Si wafer, degassed under vacuum, cured at room temperature for 4 h, and post cured at 80 °C for 2 h and 100 °C for 1 h. Finally, the Ecoflex was cooled down to room temperature and carefully peeled off from the Si wafer.

Fabrication of free-standing cellular microstructures. The free-standing cellular microstructure was obtained by precoating the glass slides with polyvinyl alcohol (PVA) as a sacrificial layer which can be washed off in water to release the attached LCP cellular film after demolding. The coating was done by spin coating the clean glass slide with a 3 wt% PVA water solution and then baking at 120 °C for 2 h to evaporate the residual water. After fabrication of the microstructure with such coated glass substrates and demolding from the PDMS, the sample was immersed in room temperature water overnight to dissolve off the PVA and release the cellular film from the glass (such dissolving process can be facilitated with hot water). The bottom LCP layer of the cellular film can be further etched to make it thinner for a higher deformability and compliance using oxygen plasma (Diener, Model: Femto PCCE).

Global topological transformation was done simply by adding ~50 μL droplet of liquids with commonly used plastic pipettes onto a 1 cm × 1 cm cellular film to immerse the structure fully and waiting for it to dry under ambient conditions. The applied liquid needs wet the structure (wetting angle > 90°) to form concave meniscus lines for the assembly to happen. For a sufficient swelling and softening of the materials, the liquid should be able to enter the cells of the microstructure and infiltrate into the polymer matrix. Note that the size and final thickness of the solvent play a role in determining the size of the area being transformed and the speed/timing of the transformation.

Localized topological transformation was done by adding small amount of liquid with a 0.5-10 μL micropipette to a large area film. Only the area that is in contact with the liquid will be assembled/disassembled.

Particle trapping is realized through topological transformation of the cellular structures to selectively trap particles with diameters that can be geometrically accommodated by the lattice compartments, while excluding particles that are larger. In particle trapping experiments, spherical particles (silica gel spherical, purchased from Sigma-Aldrich) with diameters ranging from 40 μm to 70 μm were randomly scattered on the triangular cellular surface. The triangular lattice has an edge length of 100 μm and thickness 7 μm, resulting in chambers that can accommodate spherical particles up to 50 μm in diameter. Particles with diameter < 50 μm fell into the compartments and were then engulfed and trapped under the newly formed node upon reconfiguration. On the other hand, the particles with diameters > 50 μm were washed away by the added liquid. The trapped particles can subsequently be released upon disassembly of the cellular structure by a liquid mixture of ethanol and DCM.

Surface resilience is characterized by the coefficient of restitution e, which is the ratio between relative velocity after and before the collision. In this work, we used the ball bouncing test to measure e. Specifically, steel balls with mass 0.027 g, 0.054 g, 0.104 g and 0.166 g are released from an initial height of h_0= 50 mm. Their bouncing height was recorded as h_1. Since the velocity of the ball before the collision is proportional to $\sqrt{h_0}$ and the velocity of the ball after the collision is proportional to $\sqrt{h_1}$, the coefficient of restitution is calculated by $e = \sqrt{h_1/h_0}$.

Band gap structures of the cellular structures before and after transformation is calculated via finite element simulations. We focus on the representative volume element (RVE) taken from the cellular structure. We assume the elastic wave propagates in the upper part of the structure and therefore use a plane-strain model for our analysis. Commercial software COMSOL 5.3a was used to perform the Bloch-Floquet analysis with Bloch boundary conditions applied to the boundary of the RVE. We scanned wave vectors on the Γ–M–K–Γ boundary of the irreducible Brillouin zone to obtain the dispersion relation or the so-called band structure. Since band structures depend on the geometries of the considered cellular structure, one can tune the band by transforming the structure.

Water sliding angles of the microstructured surface before and after reconfiguration were measured on a Drop Shape Analyzer (Kruss GmbH DSA100). 40 μL of MilliQ water droplets were slowly dispensed on to the structured film. The roll-off angle was measured using a droplet size of 40 μL, and the stage was tilted at a tilt rate of 0.5°/s. The averaged roll-off angle was measured at three different positions on the sample set and were confirmed across different sets of samples. Additionally, the same experiments were performed on a flat LCP thin film before and after the solvent treatment. No noticeable changes in the roll-off angle and were observed, suggesting that the change in wettability originated from the structural change rather than the chemical nature of the polymer.

Surface friction was measured as a function of a sliding angle using a 4 mm acrylic disc, which was loaded with steel ball bearings of various masses. To measure the angle, a contact angle goniometer (Kruss GmbH DSA100) was used with the structures placed on the sample stage. The disc, with a basket and wire loop affixed using two-part epoxy, was then lowered onto the structures at a controlled rate by replacing the traditional needle with a hook. This was done to prevent additional pressure being applied, which could result in the disk becoming adhered to the surface. The stage was then tilted at 0.5°/s, until the disk slid off the sample.

2 Theoretical model

2.1 Critical Young’s modulus

To quantitatively study the reconfiguration process and provide the upper stiffness limit for the material to undergo capillary assembly, we investigate a micro-cellular structure with the base of the structure anchored to a rigid substrate (see Supplementary Figure 1a). The structure is made of plates with edge length l, height h, thickness b, which are separated by an angle α . After the capillary assembly, only the upper portion with height h^* is coalesced since the bottom of the structure is always attached to the substrate and remains triangular (see Supplementary Figure 1a). This upper portion deformation, including the stretching and folding of the walls, dominates the total elastic energy in comparison to the bending deformation of the lower part (this assumption fails when the height of the structure h is too small relative to the edge length l). Therefore, the total elastic energy of one edge after the reconfiguration can be approximated by that of the upper part. The elastic energy of the deformation of the upper part includes two major components: stretching and folding (extreme bending) of the walls. In Supplementary Figure 1b, we use the triangular-to-hexagonal transformation as an example to demonstrate the stretching and folding of a single wall and such schematic is general for structures with other angles and topologies.

Energy associated with stretching: When the liquid is added to the system, the length of the walls increases from l to $l_{wet} = l(1+\delta)$, where δ is the swelling ratio. However, after the capillary assembly, the walls have length $l_a = l\sec\alpha/2$ (see Supplementary Figure 1b). Therefore, the walls upon assembly are strained by $\varepsilon_s = \frac{l_a}{l_{wet}} - 1 = (\sec\frac{\alpha}{2} - 1 - \delta)/(1+\delta)$,

and the energy of a single wall can thus be approximated by

$$U_1 = \frac{1}{2}E_{wet}V_s\varepsilon_s^2 = \frac{1}{2}E_{wet}h^*lb\left[\sec\frac{\alpha}{2} - 1 - \delta\right]^2 \qquad (1)$$

where E_{wet} is the Young’s modulus of the material in the swollen state and $V_s = h^*bl(1+\delta)^2$ is the volume of the swollen wall.

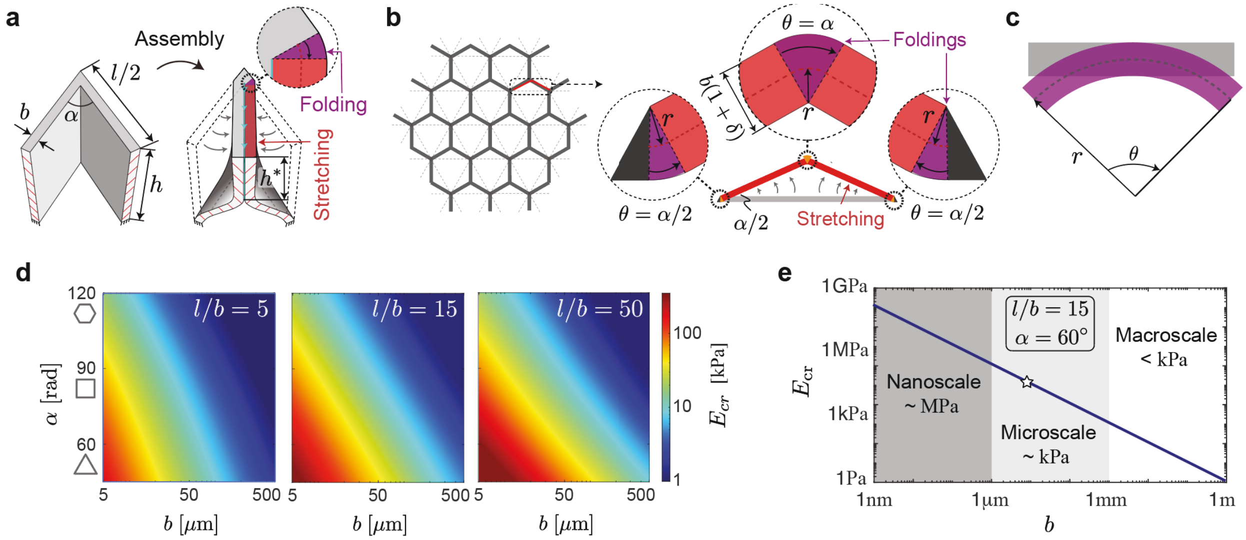

Supplementary Figure 1. Schematic presentation of the structural parameters used for a theoretical model. (a) Pre- and post-assembly configurations of a triangular compartment. (b) Components of wall deformation required for assembly. (c) Pure bending of an initially straight beam. (d) Contour plot of critical Young’s modulus E_{cr} with respect to structural parameters α and b, while the slenderness ratio is set as $l/b = 5$, 15 and 50. (e) Relation between E_{cr} and the wall thickness b predicted by our theoretical model for triangular lattices with $\alpha = 60°$. The slenderness of the lattice edges remains constant at $l/b = 15$.

Energy associated with folding: To estimate the elastic energy associated with folding we use classical beam theory. As shown in Supplementary Figure 1c, when an initially straight beam is deformed to an arch with radius r and opening angle θ, its elastic energy can be expressed as[2],

$$U_{bend} = \frac{E_{wet}I\theta}{2r} \tag{2}$$

where I is the second moment of area of the cross-section ($I = h^*b^3(1+\delta)^3/12$ in or case). As demonstrated in the insets of Supplementary Figure 1b, upon assembly the wall experiences folding at both nodes (with $\theta = \alpha/2$) and at the center (with $\theta = \alpha$). Assuming that the bending radius is half of the thickness of the swelled beam (i.e., $r \approx b(1+\delta)/2$), the total folding energy can be expressed as

$$U_2 = \frac{1}{12}E_{wet}h^*b^2(1+\delta)^2\left(\frac{\alpha}{2} + \alpha + \frac{\alpha}{2}\right) = \frac{1}{6}\alpha E_{wet}h^*b^2(1+\delta)^2 \tag{3}$$

Total elastic energy: The total elastic energy of a single wall can be obtained by summing the series associated with stretching and folding

$$U_e = U_1 + U_2 = \frac{1}{2}E_{wet}h^*\left[\left(\sec\frac{\alpha}{2} - 1 - \delta\right)^2 lb + \frac{1}{3}\alpha b^2(1+\delta)^2\right] \tag{4}$$

Work done by capillarity: The work done by capillarity can be estimated by the product of the capillary forces and the distance traveled by the meniscus, and can be expressed as[3–5]

$$W_c = \gamma h^* l \sec\frac{\alpha}{2} \tag{5}$$

where γ is the surface tension of the liquid (for a volatile liquid, such as acetone, $\gamma = 25 \times 10^{-3}$ N/m).

Critical Young's modulus: For the capillary reconfiguration to occur, the capillary work W_c must overcome the elastic energy gain U_e, i.e., $W_c > U_e$. Such simplified energy argument gives a critical Young's modulus for the underlying material:

$$E_{cr} = \frac{6\gamma l \sec\frac{\alpha}{2}}{3lb\left(\sec\frac{\alpha}{2} - 1 - \delta\right)^2 + \alpha b^2(1+\delta)^2} \tag{6}$$

The Young's modulus of the material in the swollen state E_{wet} needs to be smaller than E_{cr} to ensure the capillary assembly. In Supplementary Figure 1d, we present the contour plots of E_{cr} as functions of angle α and thickness b with respect to slenderness ratio $l/b = 5$, 15 and 50. The proposed theoretical model connects the geometry and stiffness of the polymer network with liquid characteristics, and can guide the design of reconfigurable structures.

It is worth noting that according to our model, the capillary assembly mechanism is not scale-independent. In Supplementary Figure 1e, we show how the critical Young's modulus changes as a function of the smallest dimension of the structure, i.e., wall thickness b, for a constant slenderness $l/b = 15$. According to Supplementary Figure 1e, E_{cr} changes over multiple orders of magnitude as we scale the thickness from millimeter scale down to nanometer scale — a clear indication that the behavior is not scale-independent. Specifically, at the micrometer scale E_{cr} is on the order of kPa and such a threshold can be achieved through polymer softening with properly chosen solvent. However, if the wall thickness is scaled up to millimeter scale, the polymer network needs to be softer than 1 kPa, which would normally lead to the collapse of the structure under its own weight. Moreover, since the capillary length of common liquids is around 1-3 mm, the effect of gravity would also impact the effectiveness of the capillary assembly. Therefore, the proposed capillary assembly will be less feasible for structures with their smallest dimensions beyond the micrometer scale. On the other hand, if the fabrication technique allows us to fabricate structures with nanometer scale units, the capillary assembly could work for materials with Young's moduli up to 1 GPa. This implies that for nanometer scale structures we might not need to soften the underlying material. At this scale, the capillary assembly strategy could work for more general materials that are robust against liquid, such as, plastics, carbon, or even metals.

2.2 Verification of the critical Young's modulus

To experimentally verify our model, the capillary assembly experiments were conducted on triangular cellular structures with varying geometrical parameters. Specifically, we fabricated four cellular structures using the same polymer material and the same unit size $l = 100$ μm and height $h = 70$ μm, with different wall thicknesses $b = 7$, 10, 13 and 16 μm. In Supplementary Figure 2a, we present the top view of these cellular structures after liquid evaporation. As the wall becomes thicker, it becomes more difficult for the structure to be assembled by capillary forces.

To study the assembly process more quantitatively, we measure the compartment sizes A_i for the assembled structure by tracking the grayscale of the images shown in Supplementary Figure 2a and use the blue-to-yellow color scale to indicate compartment sizes (see Supplementary Figure 2b). In Supplementary Figure 2c, we plot the distribution of the compartments over different ranges of area. We find that when the structure is completely transformed to a hexagonal lattice (for example, for structures with $b = 7$ and 13 μm) the compartment sizes are either very small (corresponding to the center of the newly formed nodes) or very large (corresponding to the hexagonal shapes). On the other hand, for the structures that fail to assemble, the compartment sizes are all mid-sized (for example structures for $b = 16$ μm). At this point, we can define an assembly index R to track the completeness of the assembly process. R is defined via the distribution of tracked compartment areas A_i as,

$$R = \frac{std[A_i]}{mean[A_i]} \tag{7}$$

where $std[A_i]$ is the standard deviation and $mean[A_i]$ is the average of the compartment areas. For a perfect assembly, where half of the compartments are near-zero size and the other half are hexagon size, we have $R = 1$, while, for the perfect (unchanged) triangular lattice, $R = 0$. The assembly index R deviates from 1 as the structure fails to completely assemble. To be more quantitatively, we define the structures with $R > 0.9$ successfully assembled and those with $R < 0.9$ fail to be assembled. For the four considered thicknesses $b = 7$, 10, 13 and 16 μm, $R = 0.99, 0.99, 0.72$ and 0.52 respectively. Therefore, the structures with $b = 7$ and 10 μm are successfully assembled and the structures with larger thickness $b = 13$ and 16 μm fail to be assembled.

Transformation for structures with different wall thickness b

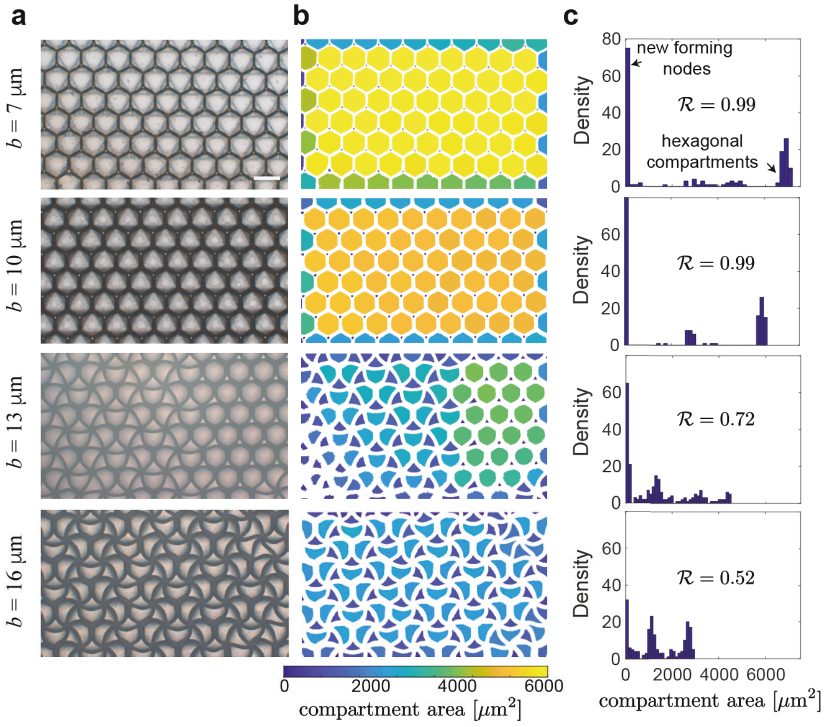

Transformation for structures with different angle α

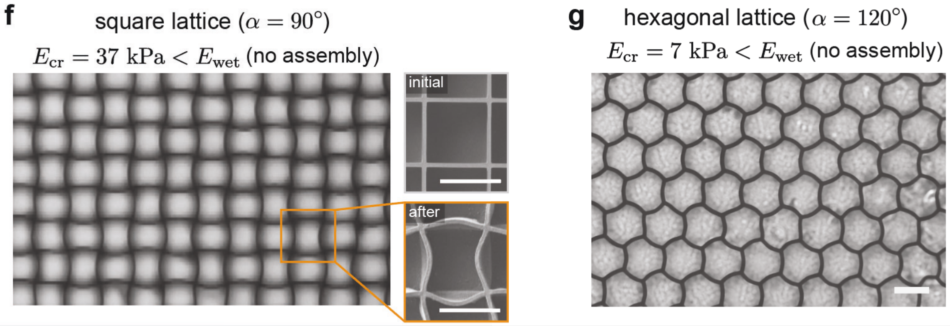

Supplementary Figure 2. Transformation of cellular structures with different wall thicknesses b and angle α. (a) Top view optical images of the liquid-treated cellular structures with thicknesses $b = 7$, 10, 13 and 16 µm, respectively. (b) Image processing to track the area of each compartment. (c) Distributions of the compartment areas and the corresponding assembly index R. (d) Critical Young's modulus E_{cr} as a function of wall thickness b. For a fixed material stiffness $E = 80$ kPa, we can derive the critical thickness $b_{cr} = 12.6$ µm. (e) Assembly index R with increasing thickness b. The predicted b_{cr} captures the critical thickness where R starts to deviate from 1 (perfect assembly). (f-g) Cellular structures with different α after liquid treatment: (f) Square lattice; (g) hexagonal lattice. The walls deform but no topological transformation occurs. Scale bars, 100 µm.

From the theoretical expression of the critical Young's modulus, we can plot E_{cr} as a function of the wall thickness b (see Supplementary Figure 2d), where again theoretically $E_{wet} < E_{cr}$ is required for assembly. Since here our polymer network is fixed with a softened stiffness of $E_{wet} = 80$ kPa and a swelling ratio of $\delta = 10\%$, the model yields a critical thickness of $b_{cr} = 12.7$ µm. For structures with $b < b_{cr}$, $E_{wet} < E_{cr}$ and the assembly will happen, while for structures with $b > b_{cr}$, $E_{wet} > E_{cr}$ and the assembly will fail. In Supplementary Figure 2e, we compare this theoretical prediction of b_{cr} with experimental measurements via image processing. The predicted b_{cr} nicely captures the transition of the assembly index R. While the two structures with $b = 7$ and 10 μm $< b_{cr}$ are fully assembled with $R \approx 1$, the structures with $b = 13$ and 16 μm $> b_{cr}$ fail to assemble. The results shown in Supplementary Figure 2e verify the accuracy of our theoretical model.

We also verify our model by testing structures with different values of α. To this end, we fabricated two cellular structures with a square lattice ($\alpha = 90°$ and hexagonal lattice ($\alpha = 120°$) geometries using the same polymer material as for the triangular cellular structure. Similarly, other geometrical parameters were kept the same as for the triangular cellular structure, with edge length $l = 100$ μm, height $l = 70$ μm and thickness $b = 7$ μm. The predicted critical Young's moduli for such square and hexagonal lattices are $E_{cr} = 37$ kPa and $E_{cr} = 7$ kPa, respectively, which are lower than the Young's modulus of the softened polymer $E_{wet} = 80$ kPa; that is, $E_{wet} > E_{cr}$. This indicates that for both square and hexagonal lattices, our model predicts that the capillary forces will not be strong enough to assemble the walls and therefore the reconfiguration will not occur. The experimental results shown in Supplementary Figure 2f-g verifies the accuracy of the theoretical prediction – although the walls buckle upon swelling, the capillary forces are not strong enough to assemble them.

2.3 Critical adhesion energy

Next, we estimate the required adhesion energy per area to hold the structure in its configuration after assembly. In the main manuscript, we have discussed how both adhesion between the walls and kinetic trapping of the polymer conformation contribute to maintain the reconfigured structure following fast evaporation of the liquid. Here we quantify how sticky the material would need to be for the structure to be held together solely by the adhesion energy. The adhesion energy of the coalesced walls can be expressed as

$$U_a = \frac{1}{2} J h^* l \ \sec\frac{\alpha}{2} \tag{8}$$

Comparing U_a with the elastic energy of the assembled structure U_e gives the critical adhesion energy per area,

$$J_{cr} = \frac{E\left[3\left(\sec\frac{\alpha}{2} - 1 - \delta\right)^2 lb + \alpha b^2 (1+\delta)^2\right]}{3l \sec\frac{\alpha}{2}} \tag{9}$$

where E is the Young's modulus of the material. In the dry state, the considered LCP has a measured Young's modulus $E_{dry} = 23{,}000$ kPa. Since the LCP is completely dried, the swelling ratio $\delta = 0\%$. In this case, with $E = E_{dry}$, Eq. (9) gives an approximate critical adhesion energy per area of $J_{cr} \approx 3.3$ joule/m^2 that is higher than the adhesion energy of typical polymer materials. In the wet state, the LCP has $E_{wet} =$ 80 kPa and $\delta = 10\%$ and therefore yields a critical adhesion energy $J_{cr} = 1.5\times10^{-3}$ joule/m^2, which is lower than that of typical polymer materials[6,7].

3 Supplemental Results & Figures

3.1 Cellular structures of low Young's modulus materials

Cellular structures made from Ecoflex^{TM} 00-10 (Young's modulus ~50 kPa) and Ecoflex^{TM} 00-50 (Young's modulus ~250 kPa) were fabricated following the general curing procedure for Ecoflex elastomers (SI section 1). However, for both material systems the structures were distorted after being peeled off from the negative silicon master due to insufficient rigidity and stickiness of the polymer-containing free siloxane species.

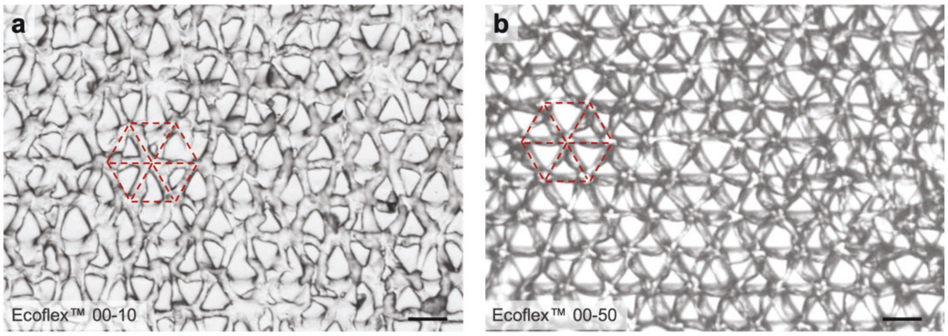

Supplementary Figure 3. Distorted triangular lattices made of (a), Ecoflex^{TM} 00-10, and (b) Ecoflex^{TM} 00-50 after being peeled off the silicon master. Scale bars, 100 μm.

3.2 Synthesis of liquid crystalline polymer (LCP) microstructures

The reactive LC monomer mixture was prepared by dissolving 96.5 mg of monomer **1**, 1.5 mg of HDDA crosslinker **2**, and 2 mg of Darocur®1173 (Supplementary Figure 4a) in roughly 1 mL of anhydrous dichloromethane (DCM). The dissolved chemicals were mixed thoroughly and dried over a cleaned microscopy glass slide (washed with water, acetone, isopropanol, and then blow-dried under nitrogen) to yield the crystallized reactive mixture for polymerization. The phase behavior of the reactive LC monomer mixture was studied with differential scanning calorimetry (DSC) using Thermal Analysis DSC Q200 with a rate of 10 °C/min. The reactive mixture showed a melting point at 42 °C and nematic to isotropic (T_{NI}) phase transition at 62 °C, as shown in Supplementary Figure 4b. The polymerization temperature was set to 120 °C where the mixture is in the isotropic phase to give a polydomain material.

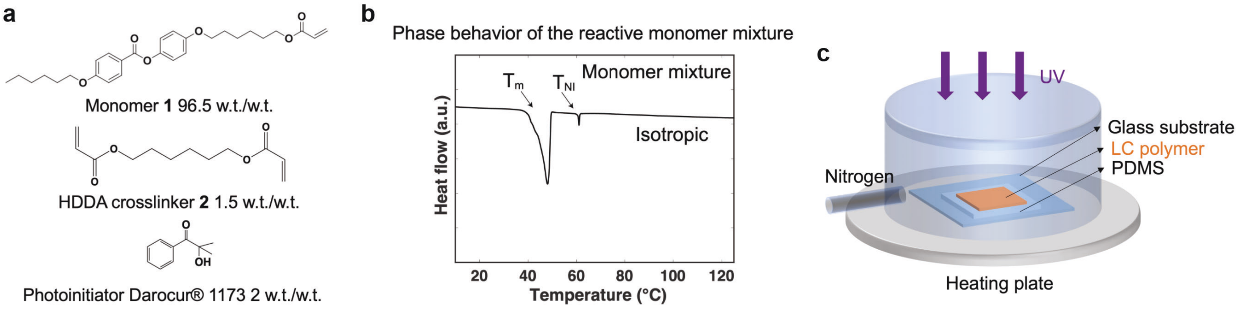

Supplementary Figure 4. Synthesis of LCP. (a) LCP chemical constituents. (b) Phase diagram of the reactive LC monomer mixture. The heating rate of the differential scanning calorimetry (DSC) was 10 °C/min. (c) Schematic of the polymerization setup.

The Si master with designed geometries (edge length $l = 100$ μm, height $h = 70$ μm and thickness $b = 7$ μm) and the negative PDMS mold were fabricated following the procedure described in SI section 1 and characterized with scanning electron microscopy (SEM).

To synthesize the LCP microstructures, we applied ~20 mg of the reactive mixture into a PDMS mold and covered the mixture with a glass substrate. The sample was heated to 120 °C (isotropic phase) and exposed to UV (Dymax Model 2000 Flood UV Curing System, light intensity of ~18 mW/cm^2) under a nitrogen atmosphere to initiate polymerization. After 20 min of polymerization, the sample was cooled down to room temperature, and the PDMS mold was carefully peeled off from the LCP microstructures.

3.3 Characterization of material properties

3.3.1 Swelling and trapping of an LCP microplate

The swelling ratio and the kinetic trapping of the LCP were tested on a microplate with the same dimensions as the lattice structure ($l = 100$ μm, $h = 70$ μm and $b = 7$ μm) to assure comparable dynamics and kinetics of evaporation. The structure was first treated with acetone and observed under an optical microscope. However, the microplates collapse upon evaporation due to the capillary force which hinders the accurate measurement of the swelling ratio of the liquid to LCP as well as the investigation of freezing dynamics. To avoid the collapse of the microplates and remove the capillary forces generated during acetone evaporation, ethanol was introduced to provide an inert liquid environment. Since ethanol does not swell the polymer, the presence of ethanol does not affect the swelling and trapping dynamics significantly and acts primarily to avoid the formation of menisci. The LCP microplate was then treated with acetone in the presence of an ethanol environment (manuscript Fig.1f): as the liquid penetrates the polymer network, the opaque glassy polymer turns clear and bright, indicating a glassy-to-rubbery transition upon swelling. The microplate was swelled to a 10 % strain along the length of the top edge. After the evaporation of acetone, the plate was trapped with a 9 % strain. Furthermore, when heated up to 70 °C (above its glass transition temperature $T_g = 58$ °C), the elongated microplate relaxed back to its initial length, confirming the kinetic nature of the trapping mechanism (Supplementary Video 1).

3.3.2 Glass transition temperature of LCP in the dry and wet states

The phase behavior of the LCP in the dry and wet states was studied with differential scanning calorimetry (DSC) using Thermal Analysis DSC Q200 with a rate of 10 °C/min. The dry LCP showed a glass transition temperature (T_g) of ~58 °C (Supplementary Figure 5a). When immersed in acetone, the fully swollen wet LCP showed a drastic decrease in T_g to –30 °C (Supplementary Figure 5a).

3.3.3 Young's moduli of LCP in the dry and wet states

The Young's moduli of the dry and wet LCP were obtained through nanoindentation measurements conducted by atomic force microscopy (AFM). By analyzing the slope of the force-displacement curves, the Young's moduli of the LCP material were determined for 4 states: (1) in its original dry state, (2) after it is fully swollen in acetone (nanoindentation measurements were conducted completely in liquid acetone environment), (3) within tens of seconds after the evaporation of acetone from the surface, and (4) after the sample was left to dry for 30 min. Supplementary Figure 5b shows that the dry LCP has a Young's modulus of ~23100±2400 kPa; it softens by three orders of magnitude to 80±19 kPa in the swollen state, and fully recovers its initial stiffness of 24000±5500 kPa after drying. Moreover, the Young's modulus does not continue to change after drying for 30 min, suggesting that the material fully regains its stiffness within ~30 s after the evaporation of the liquid from the structure.

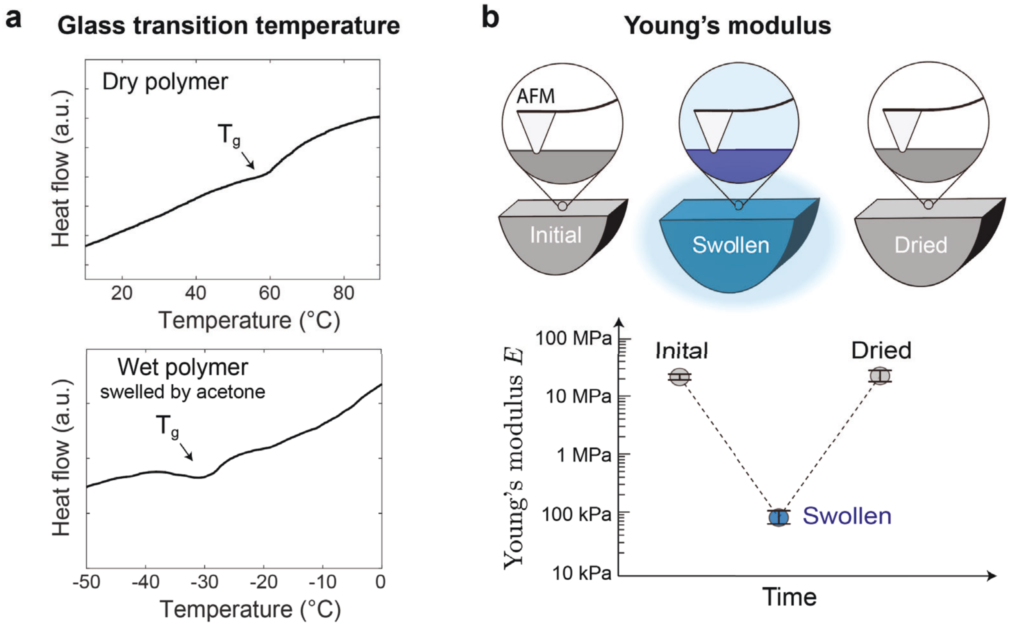

Supplementary Figure 5. Characterization of material properties of LCP. (a) Phase diagrams of the LCP polymer. Dry LCP polymer and wet LCP polymer swollen with acetone. The heating rate of the differential scanning calorimetry (DSC) was 10 °C/min. (b) Young's modulus characterization of the LCP upon swelling and drying. AFM was applied to measure the Young's moduli of the polymer on a cellular structure in the original dry state, fully swollen state, and dried state after evaporation of the liquid.

3.3.4 Systematic study of the swelling behavior of LCP with different liquids[8–11]

Water and a range of organic liquids with different polarities, volatilities, and solution parameters were selected to study the swelling behaviors of the LCP cellular microstructures. Based on their different intermolecular interactions with the LCP matrix, these solvents can be classified as good solvents, including acetone, dichloromethane (DCM), and toluene, and poor solvents, including water, ethanol, isopropanol, and hexane. Droplets of different liquids (~50 μL for a ~1 cm^2 sample, in excess of the amount required to swell the LCP to a saturated state) were placed on horizontally oriented substrates and allowed to evaporate under ambient conditions. The immersing, swelling, and drying of the cellular structures were monitored by optical microscopy. As the LCP material is hydrophobic, water does not wet the microstructure and cannot permeate into and swell the polymer matrix (Supplementary Figure 6,i). As discussed in SI section 3.3.1 for an isolated microplate, ethanol wets but does not swell the cellular microstructure; as discussed in the main text, this behavior allows it to be used as an inert solvent to enable control over the disassembly process. Isopropanol and hexane swell the structure mildly, such that the induced softening is not sufficient to trigger the assembly. DCM and toluene swell the polymer to such a large extent that the whole LCP film ruptures and delaminates from the glass substrate. It is worth noting that a mixture of different solvents can be used to trigger capillary assembly and vary the extent of the reconfiguration by controlling the swelling ratio. In addition, adjusting the crosslinking density of the polymer also offers a simple control to modify the material's mechanical properties, swelling ratio, trapping strain, and interfacial adhesion, and thus the extent and reversibility of the lattice transformation.

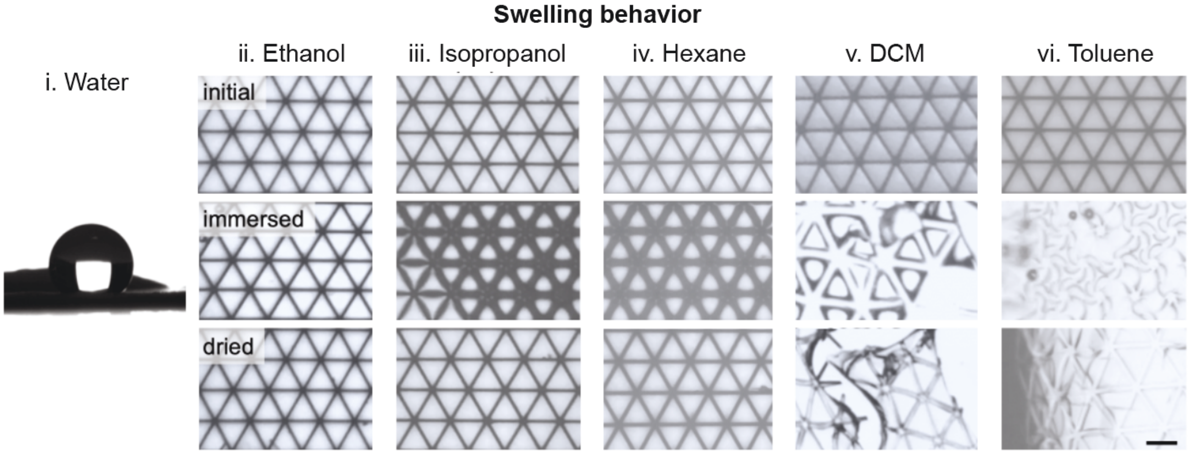

Supplementary Figure 6. Swelling behavior of LCP with different liquids. Snapshots of LCP cellular structures in the initial state, during immersing in liquids, and after evaporation of liquids. (i) Water neither wets nor swells the structure and remains in a hydrophobic state (contact angle, left ~130°, right ~130°) suspended on the surface, as shown by the optical micrograph of a 20 μL droplet sitting on the cellular film. No transformation occurs. (ii) Ethanol wets the structure but does not swell the LCP noticeably. The structures remain stiff and are not assembled upon ethanol evaporation. (iii-iv) Isopropanol (iii) and hexane (iv) wet and swell the structure slightly but not sufficient to trigger assembly upon evaporation. (v-vi) Dichloromethane (v) and toluene (vi) wet and swell the structure, but the swelling ratio is so large that the LCP films rupture and delaminate from the glass substrate. Scale bar, 100 μm.

3.4 Characterization of the topological transformation

3.4.1 3D topography of the cellular structures

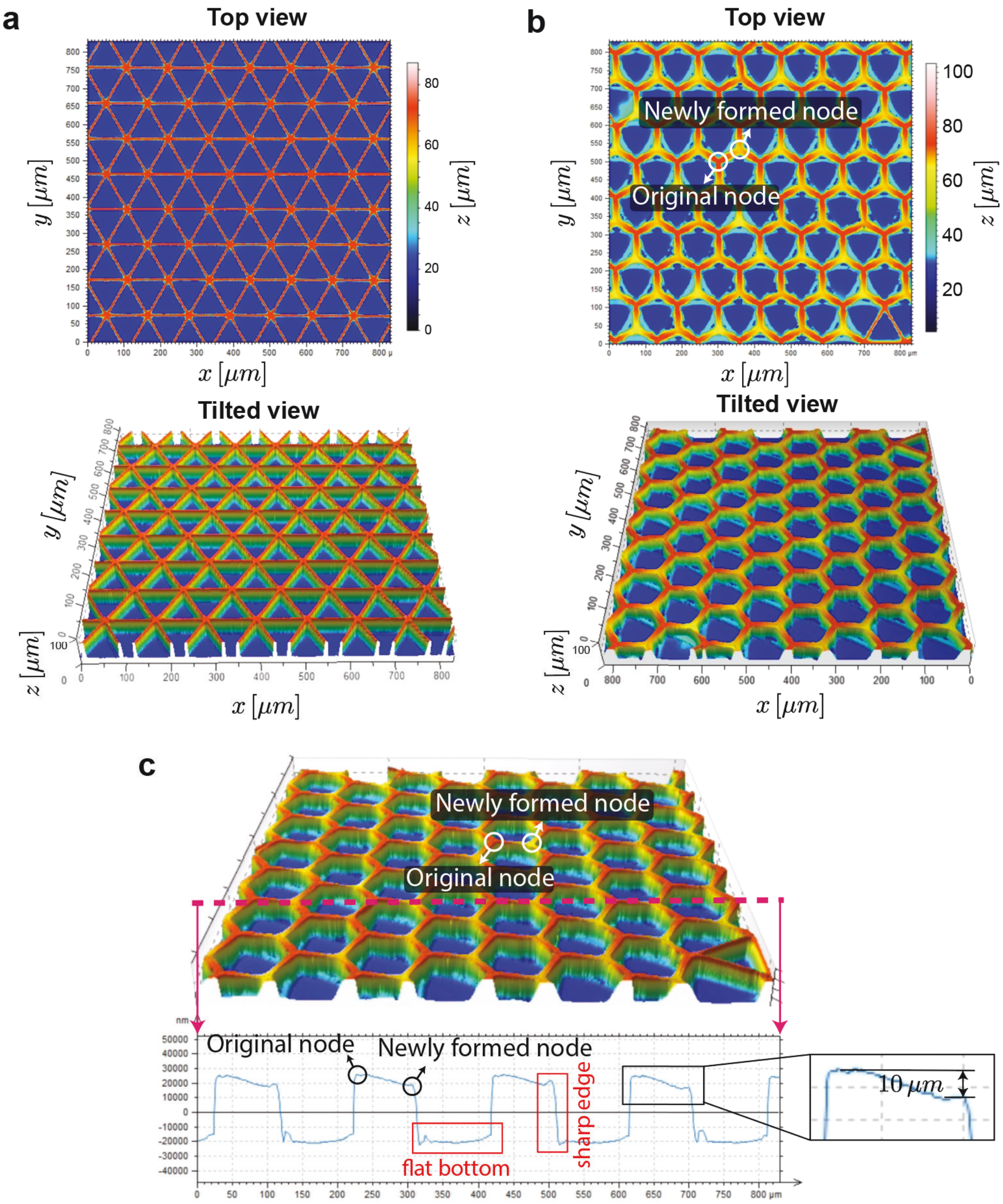

Supplementary Figure 7. 3D topography of the cellular structures. (a-b) Top and tilted view of the optical profilometer measurements showing the reconfigured 3D shape of the (a) initial triangular lattice and (b) assembled hexagonal lattice. (c) The height profile of the assembled hexagonal lattice along the dashed line. The newly formed nodes are ≈ 10 µm shorter than the original nodes. Furthermore, the inset of (c) shows that the transformed hexagonal structure contains flat bottoms and sharp vertical walls, which indicates that a half of the initial triangular compartments are completely closed through the transformation.

3.4.2 Assembly process: symmetry breaking and phase boundaries

The triangular lattices consist of nodes with connectivity six, and during the reconfiguration to hexagonal lattice the nodes are transformed to connectivity three. Let us focus on a small region around a certain node of the triangular cellular structure. Upon evaporation, six menisci form between the neighboring walls. The curved meniscus surfaces generate Laplace pressure inside the liquid. If the structure is perfect and menisci are identical, the pressures on both sides of the wall are balanced and no torque is generated (see the left inset of Supplementary Figure 8a). However, such a balanced state is not stable under infinitesimal perturbation. For example, if certain walls are perturbed by a small amount due to fabrication imperfections or environmental fluctuation, the height of the liquid surfaces on two sides of the wall become different, which generate a non-zero net torque (see the right inset of Supplementary Figure 8a). Such torque further increases the perturbation and the perturbation in turn further magnifies the torque. The process goes on and on until the adjacent walls are assembled. Since assembling three adjacent walls together costs a lot of energy, the walls will always be assembled pair by pair, which at the same time transforms the node from connectivity six to three.

The transformation of node connectivity from six to three results in an equal probability of forming two phases of patterns, with the original nodes to transform to either the Y-shaped nodes (phase I) or inverted Y-shaped nodes (phase II, see Supplementary Figure 8b). Due to the integrity of cellular structure as well as the evaporation line formed by the liquid that sequentially assemble the node (see Supplementary Figure 8c), the neighboring nodes tend to select the same phase forming ordered domains. However, over large scales, the coexistence of two phases inevitably leads to phase boundaries in between (see Supplementary Figure 8d).

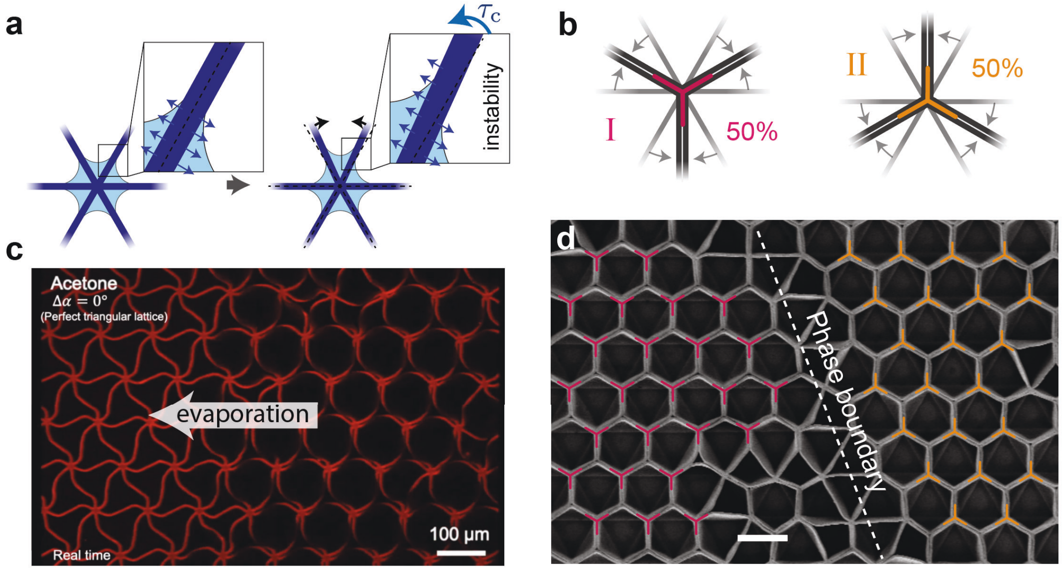

Supplementary Figure 8. Initial instability of the node and domain boundaries formation in a perfect triangular lattice after transformation. (a) A schematic demonstrating the initial instability of a triangular lattice node. (b) Two equally probable ways of transforming initial nodes leading to two different phases. (c) The evaporation line formed during transformation and the unit cells are assembled sequentially from right to left. (d) Phase boundary forms between two phases. Scale bars, 100 μm.

3.4.3 Stability of the assembled microstructures under various conditions

The reconfigured structure is maintained by both the kinetic trapping of the polymer conformation and the interfacial adhesion between the assembled walls. Such dual protection enables the robustness of the assembled microstructures under various harsh conditions. For example, the structures remain assembled when heated up to 130 °C (see Supplementary Figure 9a-b). Although heating above T_g overcomes the kinetic trapping and relaxes the polymer conformation, the material becomes sticky and more importantly it becomes much softer due to increased molecular mobility – similar to the swelling-induced rubbery state (plasticizing with solvents) that has a Young's modulus of ~80 kPa. If we assume that both cases have similar Young's moduli, it then requires only an adhesion energy of 1.5×10^{-3} joule/m^2 to hold the reconfigured structure (see discussion in SI section 2.3). Only a slight bulging of the assembled walls was observed at 130 °C due to the thermal expansion of the LCP materials upon heating. Furthermore, the assembled structures stay robust after being immersed in a poor solvent such as ethanol for a few days, indicating that, although ethanol may be able to decrease (but not fully eliminate) the adhesion energy between the assembled walls, it cannot enter the polymer network to alter the conformation of the polymer chains at the molecular scale, and therefore cannot disassemble the microstructure (Supplementary Figure 9c).

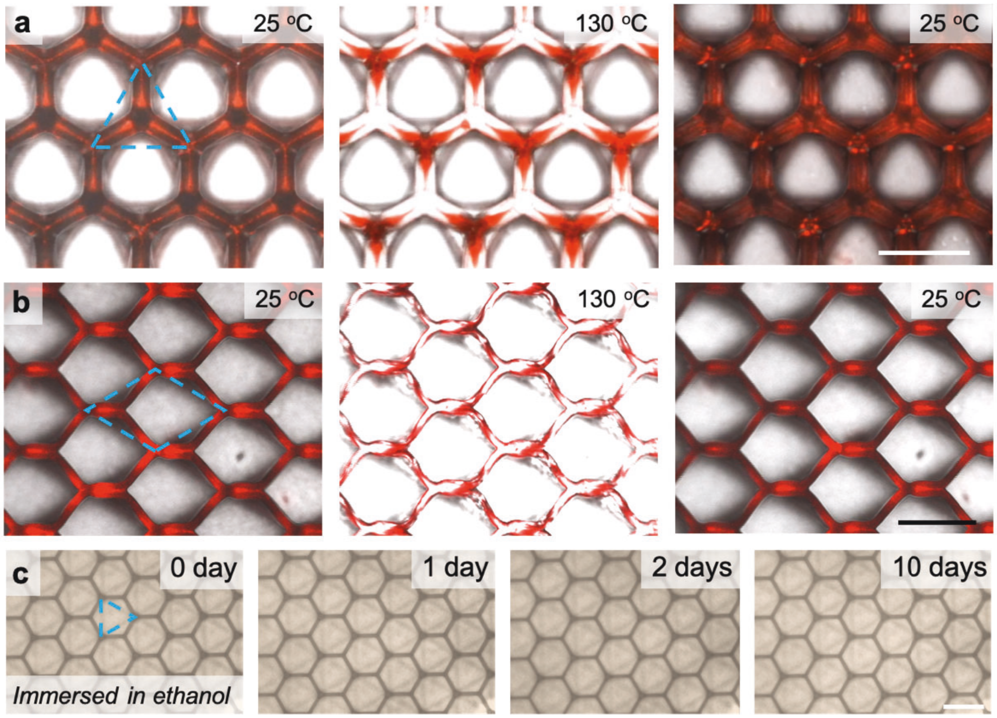

Supplementary Figure 9. Stability of the assembled microstructures under harsh conditions. Confocal microscopy images of the assembled structure for (a) a triangular-to-hexagonal system and (b) a diamond-to-hexagonal system, at room temperature (left), heated to 130 °C (middle), and cooled to room temperature (right). The structure is locked in a fully assembled configuration throughout the heating and cooling process. (c) Optical microscopy images of the assembled structure after immersion in ethanol for 0 day, 1 day, 2 days, and 10 days post assembly. Scale bars, 100 μm.

3.4.4 Reversibility and fatigue test

To test the reversibility of the transformation, ten back-and-forth repeated cycles of transformation on the same cellular structure was conducted (Supplementary Figure. 10a). No noticeable fatigue behavior was observed. As shown in the zoomed-in image, the walls remain clearly separated around the node after the 10th disassembly. We note that fatigue may occur with more transformation cycles, and it is expected to first show at the hinges due to large deformations near the node.

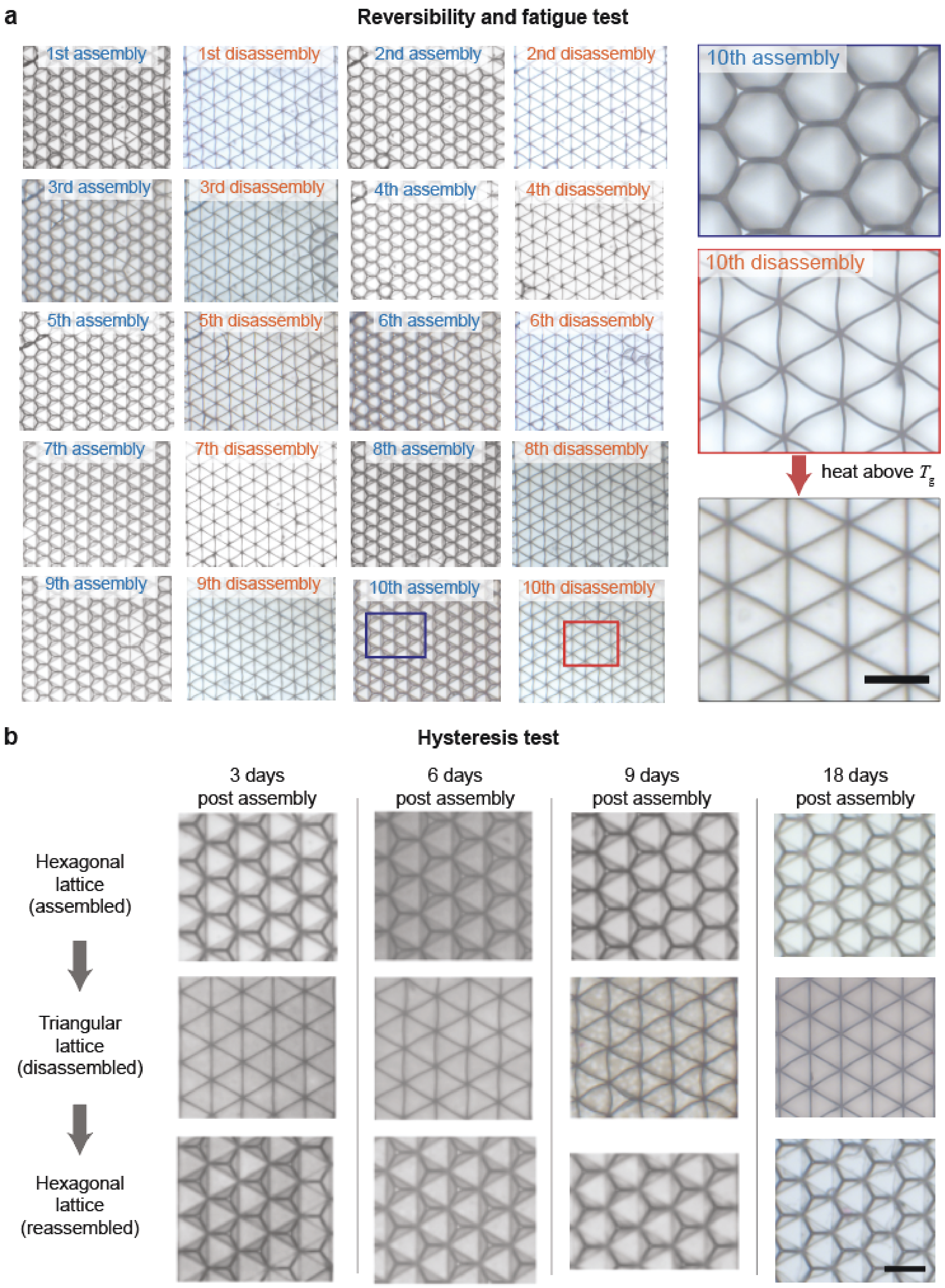

Supplementary Figure 10. Reversibility, fatigue and hysteresis test with LCP (2wt% HDDA). (a) Reversibility and fatigue test over ten cycles. (b) Hysteresis test over time breaks of 3, 6, 9 and 18 days.

3.4.5 Hysteresis test

The hysteresis behavior of the reversibility of the transformation over long time breaks was tested over 3, 6, 9, and 18 days, and no noticeable hysteresis was observed (Supplementary Figure. 10b). Specifically, the transformed structure was kept under its hexagonal configuration for a long period (3, 6, 9, and 18 days), and then subjected to disassembly and assembly process. The structure was shown to be capable of complete disassembly and assembly over at least an 18-day break.

We note the potential 'sticky' problems over very long periods after transformation in systems with polymer films in close contact. The hysteresis tests showed that a slightly higher concentration of DCM might be required for a larger swelling sufficient to peel apart the assembled walls as compared to freshly assembled structures, due to an increase in the interfacial adhesion. Furthermore, different crosslinking densities of the polymer may affect the hysteresis behavior. With a lower crosslinking density, the polymer is likely to be stickier and is more vulnerable to hysteresis during repeated transformation. For the purpose of robust reversibility, we choose the crosslinking density of LCP within a range of 1.5 to 3wt%.

3.5 Generalization of the proposed principle of topological transformation

3.5.1 Other lattice geometries

Our theoretical model predicts that the capillary forces prefer to assemble edge pairs with smaller angles. Addition geometries are designed and experimentally tested based on this general principal (Supplementary Figure 11). It is important to note that geometrical compatibility also needs to be taken into account when considering certain lattices, such as the diamond lattice (shown in manuscript Fig. 3a, iv). If both small angles at the rhombus nodes were closed, the transformed nodes would fail to repack into a connected lattice due to geometrical frustration. Under this circumstance, one of the smallest angles at each node has to open up to be compatible with other nodes, which results in a hexagonal lattice.

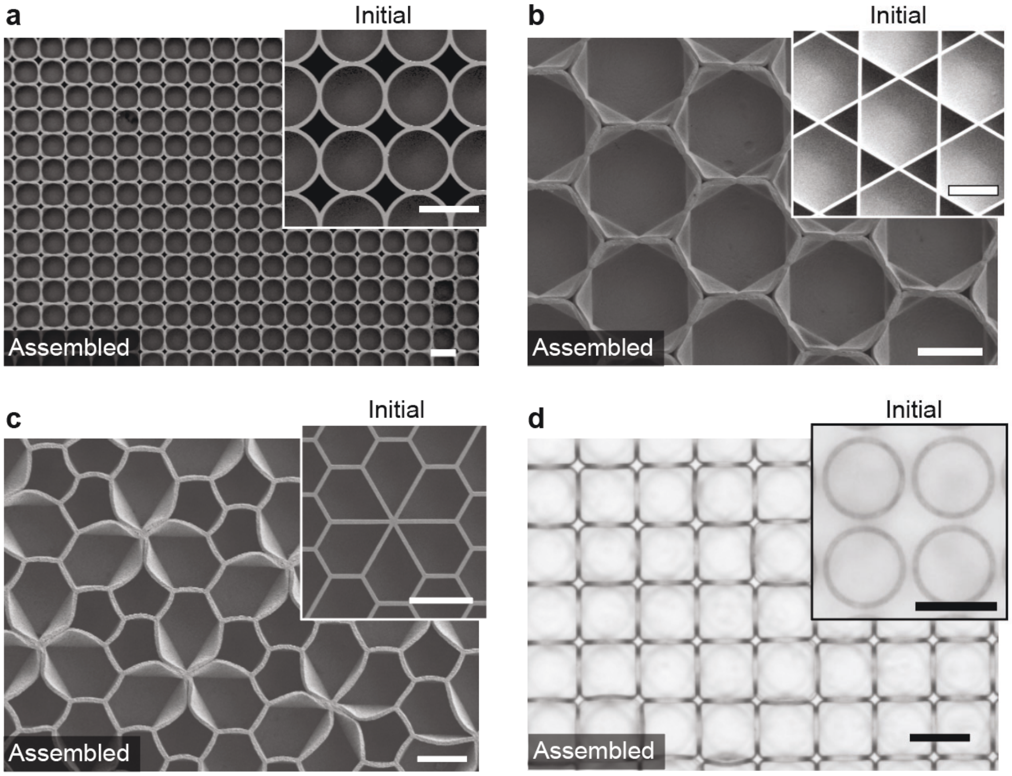

Supplementary Figure 11. Topological transformation of complex lattice geometries in large areas. (a) Circular lattice (inset) transformed to a square lattice. (b) Initial kagome lattice (inset) transformed to a hexagonal lattice. (c) Transformation of flower-patterned lattice. Scale bars, 100 μm. (d) Initial isolated rings transformed to an interconnected square lattice. When the top surface is coated with conductive materials, such transformation could be potentially used to alter the conductivity of the cellular structures. Scale bars, 30 μm.

3.5.2 Other structural dimensions

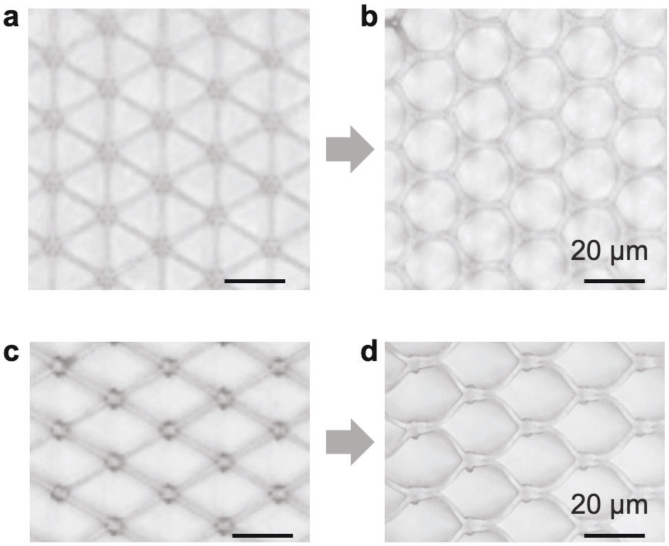

Supplementary Figure 12. Topological transformation of cellular structures with edge length $l = 20\ \mu m$, $b = 2\ \mu m$, and $h = 10\ \mu m$. (a) Initial triangular lattice and (b) assembled hexagonal lattice. (c) Initial diamond lattice and (d) assembled hexagonal lattice. These results prove that, as predicted by our theoretical model (Supplementary Figure 2), our strategy is applicable to smaller scales. Scale bars, 20 μm.

3.5.3 Other materials

3.5.3.1 Poly(2-hydroxyethyl methacrylate) (PHEMA)

The generality of the transformation strategy to other materials was successfully demonstrated with poly(2-hydroxyethyl methacrylate) (PHEMA) crosslinked by 1 wt% of ethylene glycol dimethacrylate (EDGMA), as shown in Supplementary Figure 13a. The PHEMA was synthesized following a reported procedure with adjusted chemistries[12]. The polymer precursor was prepared by mixing 1 mL 2-hydroxyethyl methacrylate (HEMA, Sigma-Aldrich) with 20 μL EDGMA and 10 μL Darocur®1173. The mixture was casted on to the PDMS mold and covered with a glass slide, and then exposed to UV light (Dymax Model 2000 Flood UV Curing System, light intensity of ~18 mW/cm^2) for 1.5 min. The mold was carefully peeled off to yield the PHEMA microstructure. Droplets of acetone were used for triggering the transformation. We note that a longer curing time may result in a denser polymer network and a different liquid will be needed for sufficient softening effect.

3.5.3.2 Molecularly aligned side-on LCP

Hierarchical deformation of the cellular structures was achieved by imprinting the material with anisotropic thermal responses from aligned LCPs. Here we present the results using a different LCP material from the one described before – a side-on LCP shown in Supplementary Figure 13b with LC mesogens aligned following a procedure we reported recently[13]. The reactive monomer mixture was prepared following the procedure in SI section 3.2. For the alignment and polymerization, 20 mg of the reactive mixture was applied into a PDMS mold and covered with a glass substrate. The sample was then placed in a magnetic field generated by a NdFeB-based magnet with surface field of 0.5 T (Supplementary Figure 13b), heated to 80 °C (isotropic phase), cooled down to 60 °C at a rate of 1 °C/min. The UV polymerization was conducted following the same procedure described in SI section 3.2. Droplets of acetone and DCM (2:1) mixtures were used for triggering the transformation.

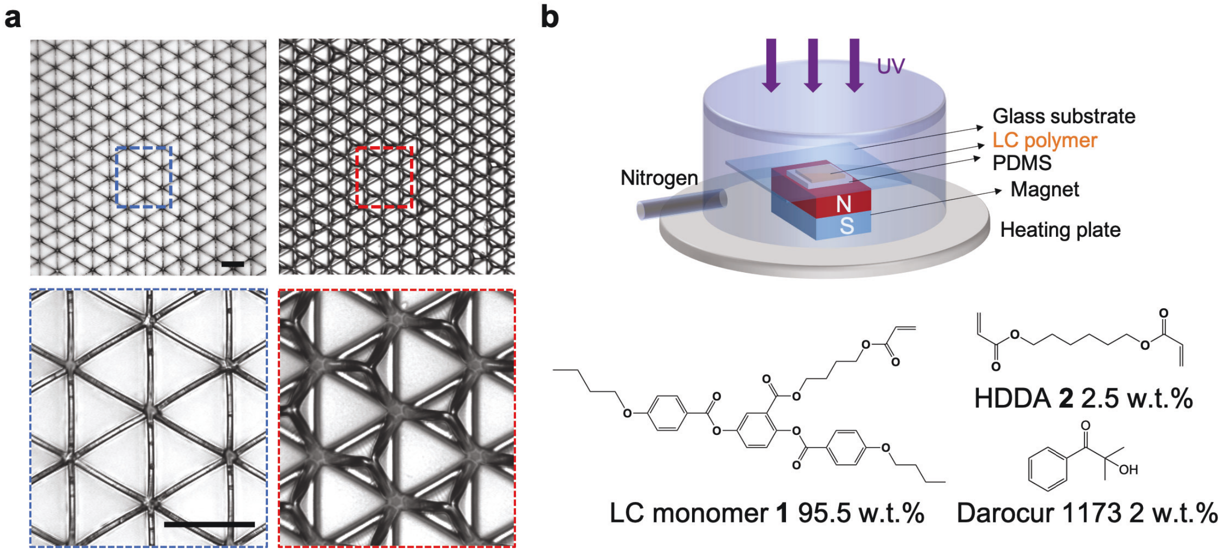

Supplementary Figure 13. Application to different polymeric materials. (a) Topological transformation of a poly(2-hydroxyethyl methacrylate) PHEMA triangular cellular lattice to a hexagonal lattice. Scale bars: 100 μm. (b)

Schematic of the experimental setup (top) and LCP chemical constituents (bottom) for the synthesis of molecularly aligned nematic LCP.

3.6 Free-standing cellular structures

In Supplementary Figure 14, we show the microscopic image of a free-standing cellular film with a triangular lattice. After liquid treatment, part of the initial triangular lattice is transformed to a hexagonal one. However, since the thin cellular film cannot hold any force or moment, the film is warped and curled by the liquid during the transformation. It indicates that the substrate anchoring guarantees the stability of the cellular structure so that the transformation is immune from global floppy deformations. Application-wise, a firm substrate also provides strong support to the cellular structures, which in turn possess characteristic surface properties. Additionally, without the anchoring from the substrate, floppy lattice geometries such as square and rhombic lattices will collapse or assemble chaotically (Supplementary Figure 14d).

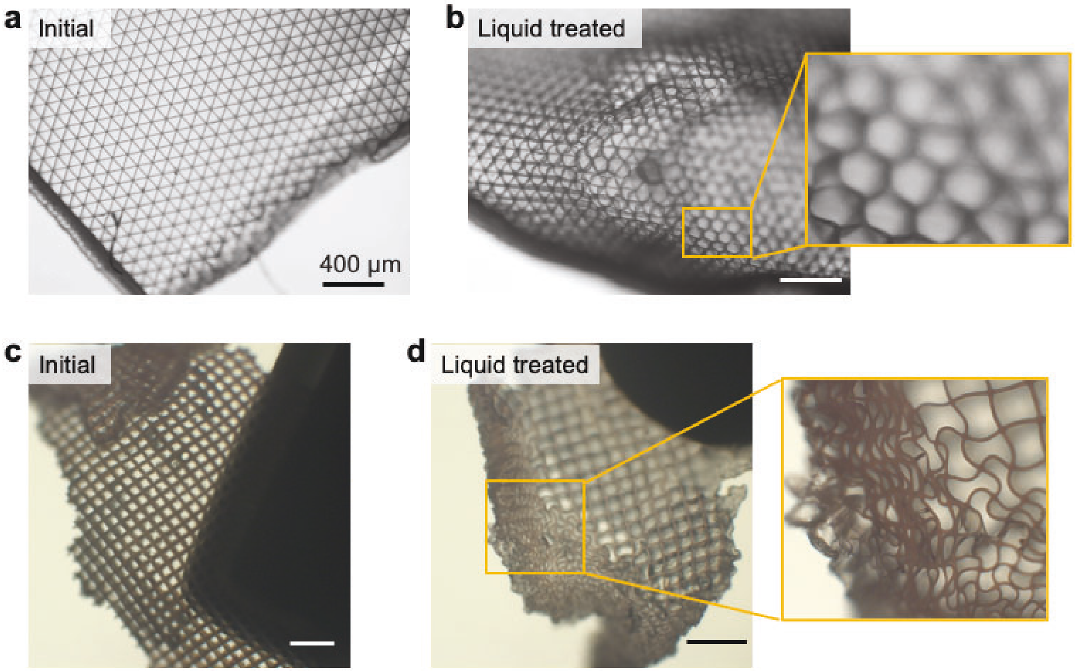

Supplementary Figure 14. **Free-standing cellular film.** (a-b) The free-standing triangular cellular mesh with soft deformable substrate: (a) initial structure upon exposure to liquid (acetone); (b) partially assembled structure after the evaporation. (c-d) The free-standing square cellular mesh with soft deformable substrate: (c) initial structure; (d) after the evaporation, the structure assembled chaotically and deformed globally due to the floppy nature of a free-standing film.

3.7 Local transformations with small droplets

Localized transformations can be achieved by applying a small amount of liquid to a large sample, such that only the area that is in contact with the liquid will be transformed (see Supplementary Figure 15). Such localized control of transformations could be potentially used for area-specific applications. Due to the compartmentalized nature of the cellular structure, the applied liquid will tend to fully fill a certain number of cells rather than spreading to larger areas with partially filled cells. Therefore, the thickness of the applied solvent drop can be considered as no shorter than the cell height in most cases. As shown in Supplementary Figure 15a albeit complete transformation in a ~ 500 μm × 500 μm area. By varying the volume of the liquid applied, local topological transformations with different feature sizes can be realized controllably (Supplementary Figure 15a-d). Note that for some extreme cases where the liquid volume is far below 1 μL, transformation was not observed due to insufficient swelling and capillary work.

Local disassembly can be achieved with similar procedure, which enables more sophisticated local patterns through sequential assembly and disassembly. In Supplementary Figure 15e, a small droplet was first applied to a uniformly assembled hexagonal lattice that disassembled a ~ 1500 μm × 1500 μm area. Then, a ~ 500 μm × 500 μm area within this disassembled region can be assembled again by a smaller droplet yielding concentric rings of assembled and disassembled lattices. Furthermore, such local control can also be integrated with the trapped intermediate configurations described in manuscript Fig. 2g for more complex patterns and corresponding functions (Supplementary Figure 15f).

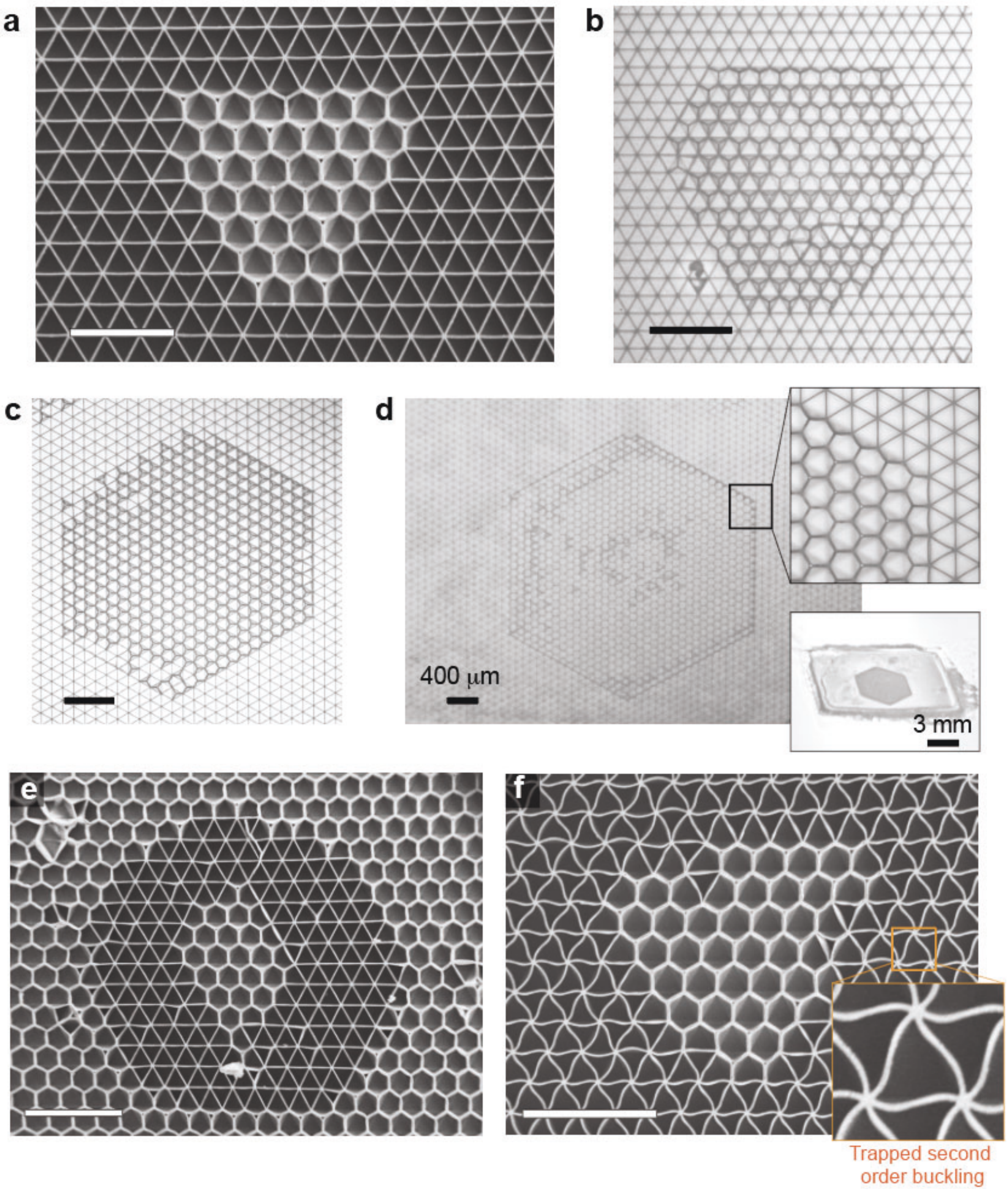

Supplementary Figure 15. Localized transformation with small droplets. (a-d) Localized transformation of the triangular lattice into a hexagonal lattice with different sizes of the applied droplets. Note that the small droplet applied tends to spread to a hexagonal shape due to the symmetry and connectivity of the initial triangular lattice. (e) Multi-step localized transformation after a sequential assembly (large area)-disassembly (medium area)-assembly (small area) process. (f) Integration of the kinetic trapping effect of buckled walls with the local transformation.

3.8 Phase design

3.8.1 Geometrical perturbations

To obtain a defect-free assembled structure, small geometrical perturbations can be introduced to the initial triangular lattice to make every node favor one phase over the other. Our theoretical model indicates that edges with smaller angles are easier to assemble than those with larger angles. Therefore, by perturbing the angles at the initial nodes by a small angle $\Delta\alpha$, we can design the structure to favor a chosen phase at every node (see Supplementary Figure 16a as an example for favor phase I). Experimentally this is realized by building structures with slightly curved walls (see Supplementary Figure 16b). Specifically, to design a node with its angles perturbed by $\Delta\alpha$, we fabricate curved walls with radius $\rho = l/\left(2\sin\frac{\alpha}{2}\right)$ and central angle $2\Delta\alpha$. We choose $\Delta\alpha = 2.5°$ where the actual difference between a lattice with curved edges and a perfect lattice is visually indistinguishable (see Supplementary Figure 16c, where the inset of shows the marginal difference of the curved triangle and the perfect triangle in terms of CAD design).

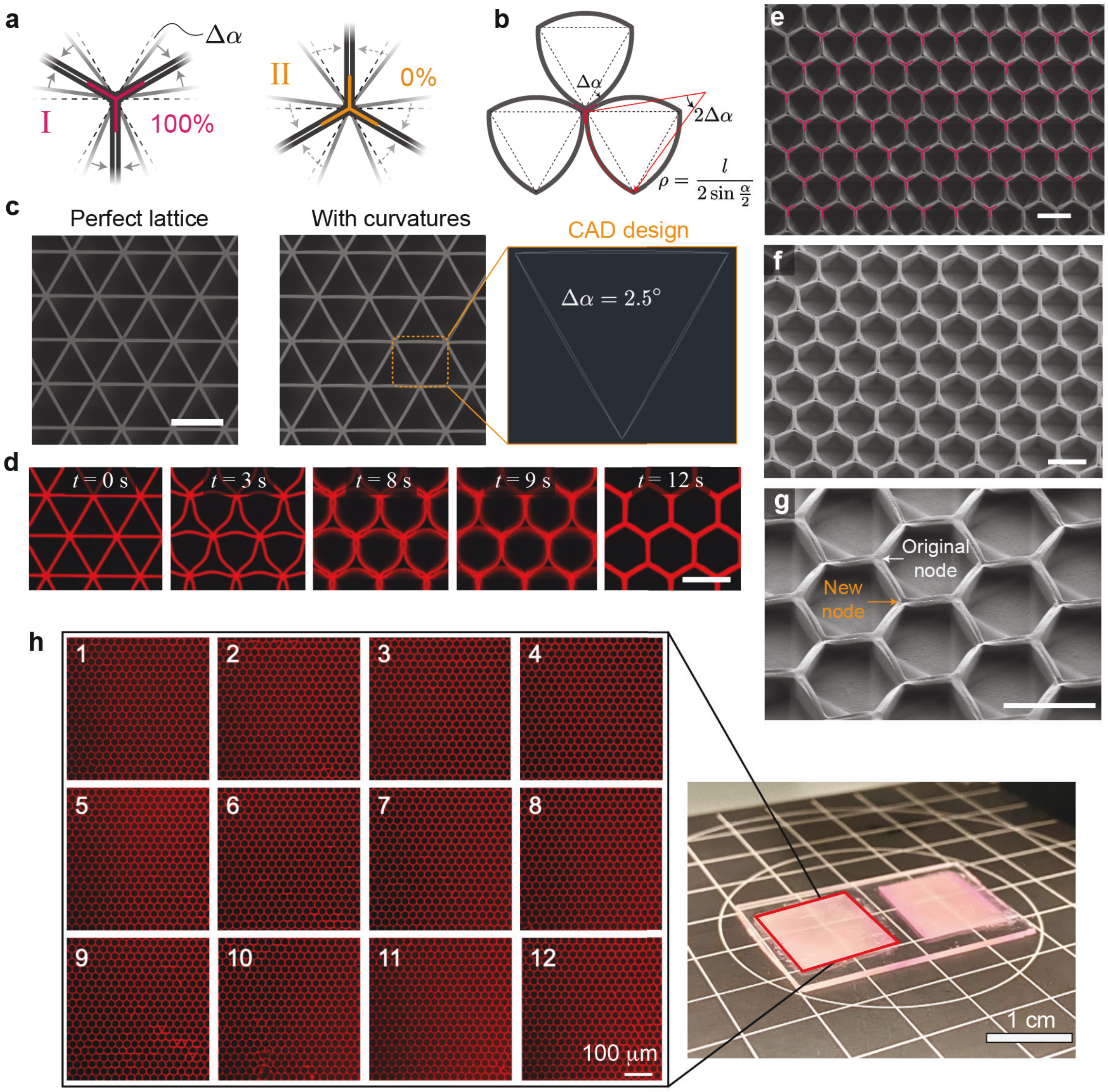

Supplementary Figure 16. Perturbation design for uniform assembly. (a) The phase selection can be controlled at each initial node by introducing a small difference in the local angles $\Delta\alpha$. (b) A schematic of the experimental design of the node to favor phase I using curved walls. The schematics exaggerate the curvature used in the experiments shown in c-f. (c) Actual structure with slightly perturbed angles $\Delta\alpha$ =2.5° (imaged by SEM). The inset shows the corresponding CAD design. The initial structure is visually indistinguishable from a perfect triangular lattice. (d) Confocal snapshots of the assembly of a perturbed triangular lattice at different time points. (e-g) Initial triangular lattice with $\Delta\alpha = 2.5°$ is transformed to a perfect hexagonal lattice with a single uniform phase without phase boundaries: (e) top view, (f) tilted view and (g) zoomed-in tilted view. Scale bars, 100 µm. (h) Large-area uniformed transformed samples (1.5 cm × 1.5 cm, much larger samples are readily accessible with molding) used for friction and wetting measurement. Homogeneous transformations are observed in every region as illustrated by twelve different regions of sample each containing roughly 20 by 20 compartments (2 mm by 2 mm in size).

The indistinguishable imperfections introduced to the triangular lattice have a profound impact during the capillary assembly. As shown in Supplementary Figure 16d when the lattice is swelled by the liquid, the buckling modes of the edges are altered by the imperfections in a way that favors Y shape nodes. The capillary forces then further zip up the closer walls to form a uniform hexagonal lattice. Supplementary Figure 16e-h show SEM, optical, and confocal microscopic images of the assembled perfect hexagonal cellular structures in large areas. No defects or domain boundaries appear in this case, due to the controlled geometrical perturbations introduced in the structure.

3.8.2 Phase boundary design

Since designing the orientation of the wall curvature enables one to program each individual node to favor either phase I or phase II (Supplementary Figure 17a), the locations of phase boundaries can be easily controlled by prescribing the distribution of the two types of angular perturbations. Fig. 17b illustrates how structures with two regions, consisting of nodes with perturbations that favor phase I or phase II, respectively, lead to an assembled lattice with domains concatenating with each other at the phase boundary, with phase I on the left and phase II on the right. Again, while the schematic in Supplementary Figure 17b shows exaggerated curvatures, the actual structures are indistinguishable from a perfect triangular lattice. It is worth noting that the specific design of the edges on the boundary does not matter, because the position of the defect is determined by the phases of bulk structures rather than the specific imperfections on the boundary. Supplementary Figure 17c shows the emergence of a phase boundary upon reconfiguration. The left part and the right part of the structure corresponding to different phases. Furthermore, such phase boundary design can be applied to form more complex patterns, as exampled in Supplementary Figure 17d as a heart pattern. We note that the large area SEM image is stitched from 4 small panels. Supplementary Figure 17e shows that the differences between two phases are optically invisible before capillary reconfiguration and become visible afterwards.

The encryption level of this method is determined by the value of perturbation curvature and the unit cell size. If a computer equipped with a high-resolution camera is able to pick up the curvature in each unit cell, then we need to increase the level of encryption by either decreasing the curvature or making the unit cells smaller. Generally, we believe that our current information encryption method cannot be easily picked up by a computer. For example, the demonstrated information encryption samples usually contain 50 by 50 unit cells. A high-resolution camera can take a picture with roughly 2000 by 2000 pixels with each unit cell described by 40 by 40 pixels. With a perturbation of 2.5 deg, the maximal deviation of the curved edge is roughly 0.01 times the unit cell length, which cannot be picked up by a 40 by 40 resolution picture. After the transformation, such subtle difference is strongly magnified by the phase boundaries that are visible even by naked eyes (see Supplementary Figure 17e). Lastly, depending on the fabrication accuracy, the perturbation angle can be further decreased to ensure stronger encryption.

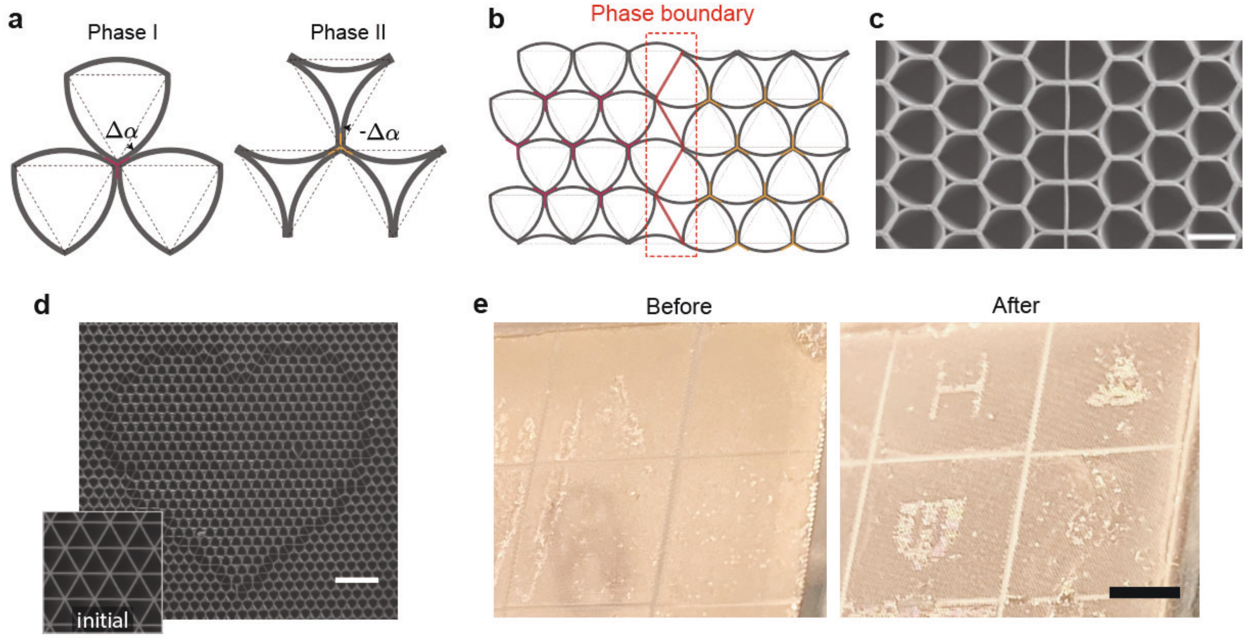

Supplementary Figure 17. Phase boundary design. (a) Schematics of two imperfection designs that lead to phase I and phase II respectively. (b) Design of a phase boundary by controlling the distribution of the two types of angular perturbations. (c) SEM image of the engineered phase boundary: the nodes on the left are designed to favor a different phase than the nodes on the right. Scale bar, 100 μm. (d) Phase designed heart pattern before and after transformation. Scale bar, 400 μm. (e) Photos of microstructures with designed phase boundaries before and after capillary reconfiguration. The boundary between the two phases is optically visible in the assembled structures. Scale bar, 5 mm.

4 Captions for Videos

Video S1: Inducible relaxation of an isolated LCP microplate and a hexagonal lattice after trapping in the deformed state.

An LCP microplate with a 9% strain along the length of the top edge can be fully restored to its initial length upon heating to 70 °C above its T_g (58 °C). The process was monitored by optical microscopy. A similar response - full reversibility of the trapped state back to the initial state - is seen for a hexagonal lattice.

Video S2: Elasto-capillary assembly of a triangular lattice into a hexagonal lattice.

A droplet of acetone is added to the triangular lattice microstructure. The applied liquid first penetrates the material and softens it substantially. As the acetone evaporates, capillary forces bend and assemble the cellular walls, transforming a triangular lattice with node connectivity of six to a hexagonal lattice with node connectivity of three. Subsequently, the fast deswelling of the polymer re-stiffens the microstructure and locks it in the stable hexagonal topology.

Video S3: Robustness of the transformed topology.

The combined effects of polymer trapping and adhesive forces make the new topology highly stable against harsh conditions. Here, the assembled structures maintain their configuration and topology when heated far above T_g.

Video S4: Disassembly of the hexagonal lattice back to the initial triangular topology.

A droplet of a 2:1 mixture of dichloromethane (DCM) and ethanol is added to the assembled hexagonal lattice. DCM first swells the polymer substantially, triggering dissociation of the adhered walls and restoring the original node connectivity of six. As the liquid mixture evaporates, DCM leaves the system first due to its higher volatility, allowing the polymer to deswell, regain its stiffness, and finally relax back to the initial triangular lattice. The less-volatile ethanol (which does not swell the polymer) remains in the system to prevent capillary forces from reassembling the walls during this process, and then evaporates only after the DCM has fully evaporated, when the walls are once again too stiff to be assembled by capillary forces.

Video S5: Hierarchical transformation of a diamond lattice by first transforming to a hexagonal topology via acetone and then inducing a phase transition of an oriented LCP.

Multi-stimuli lattice transformation of a diamond structure imprinted with z-aligned LC mesogens, first to a hexagonal structure and then to a brick structure. The first transformation is achieved by elasto-capillary assembly of the diamond lattice upon application and evaporation of acetone; the second transformation is realized by heating the sample to its nematic-isotropic phase transition temperature.

Video S6: Elasto-capillary assembly over a larger area without and with phase design.

Transformation of a perfect triangular lattice results in various types of defects, including line defects and point defects due to the fact that there exist two possible phases for each node. By introducing a small angular perturbation at each node, the entire structure can be biased to favor a single phase, and the capillary transformation results in a uniform hexagonal lattice with a single domain.

Video S7: Demonstration of properties and applications made possible by topological transformation of the cellular structures.

Three examples of properties and behaviors that emerge as a result of the topological transformation: 1) The closed chambers (formed by the bending and assembly of walls) release uniform microscale bubbles from the ordered cavities upon disassembly. 2) Ball-bouncing test results demonstrate that the resilience of the cellular surface changes significantly after the topological transformation. The triangular structure displays broken walls after impact, while the transformed hexagonal surface exhibits larger craters but no detectable structural damage. 3) The cellular surface becomes more adhesive to water droplets upon transformation. The surface of the assembled (hexagonal) lattice picks up a water droplet that is sitting on the surface of the initial triangular lattice. Conversely, the pre-assembled (triangular) surface is not able to pick up a water droplet from the post-assembled surface.

5 References:

1. Thomsen, D. L. *et al*. Liquid crystal elastomers with mechanical properties of a muscle. *Macromolecules* **34**, 5868–5875 (2001).
2. Beer, F. P., Johnston, E. R., Dewolf, J. T. & Mazurek, D. F. *Mechanics of Materials, 5th Edition*. vols 1–12 (1999).
3. Roman, B. & Bico, J. Elasto-capillarity: Deforming an elastic structure with a liquid droplet. *J. Phys. Condens. Matter* **22**, (2010).
4. Holmes, D. P., Brun, P. T., Pandey, A. & Protière, S. Rising beyond elastocapillarity. *Soft Matter* **12**, 4886–4890 (2016).
5. Wei, Z. *et al*. Elastocapillary coalescence of plates and pillars. *Proc. R. Soc. A Math. Phys. Eng. Sci.* **471**, (2015).
6. Myshkin, N. & Kovalev, A. Adhesion and surface forces in polymer tribology—A review. *Friction* **6**, 143–155 (2018).
7. Israelachvili, J. N. *Intermolecular and surface forces*. (Academic press, 2011).
8. Rubinstein, M. & Colby H. Ralph. *Polymer Physics*. (Oxford Univerisity Press, 2003).
9. Dimarzio, E. A. & Gibbs, J. H. Molecular interpretation of glass temperature depression by plasticizers. *J. Polym. Sci. Part A Gen. Pap.* **1**, 1417–1428 (1963).
10. Du, H. & Zhang, J. Solvent induced shape recovery of shape memory polymer based on chemically cross-linked poly(vinyl alcohol). *Soft Matter* **6**, 3370–3376 (2010).
11. Flory, P. J. *Principles of Polymer Chemistry*. (Cornell University Press, 1953).
12. Wu, G., Xia, Y. & Yang, S. Buckling, symmetry breaking, and cavitation in periodically micro-structured hydrogel membranes. *Soft Matter* **10**, 1392–1399 (2014).
13. Yao, Y. *et al*. Multiresponsive polymeric microstructures with encoded predetermined and self-regulated deformability. *Proc. Natl. Acad. Sci. U. S. A.* **115**, 12950–12955 (2018).